ETH zürich D ERDW

Simultaneous Estimation of Conductivity and Inducing Field in Electromagnetic Induction Sounding

Master's Thesis

Jingtao Min

jinmin@student.ethz.ch

Institute of Geophysics

Departement of Earth Sciences, D-ERDW

ETH Zürich

Supervisor:

Dr. Alexander Grayver

Co-referees:

Prof. Dr. Alexey Kuvshinov

PD Dr. Amir Khan

August 22, 2022

Contents

Abstract

Time-varying electromagnetic field observed on the ground or at a spacecraft consists of contributions from inducing electric currents, as well as induced currents in the conductive Earth's interior by virtue of electromagnetic induction. Knowledge about the spatio-temporal structure of inducing currents is a key component in ionospheric and magnetospheric studies and is also needed in space weather hazard evaluation, whereas the induced currents are sensitive to the Earth's subsurface electrical conductivity distribution and allow us to probe this physical property. This thesis presents an approach that reconstruct the inducing source and subsurface conductivity structures simultaneously, preserving the consistency between the inducing and induced currents by exploiting the physical link between them. To achieve this, the underlying inverse problem is formulated as a separable nonlinear least squares (SNLS) problem, where the inducing current and the subsurface conductivity enter as linear and non-linear model unknowns, respectively. The SNLS problem is solved with the variable projection method and compared with other conventional approaches. The feasibility of this approach is demonstrated via experiments where the ionospheric and magnetospheric currents along with a 1-D average mantle conductivity distribution are simultaneously reconstructed from the ground magnetic observatory data.

Parts of this thesis will be submitted as an article to *Earth, Planets and Space* and can be referred to as:

Min, J. and Grayver, A., Simultaneous estimation of inducing source field and mantle electrical conductivity using the variable projection approach, *Earth, Planets and Space*, in preparation.

1. Introduction

Time variations of magnetic field that we observe on the ground or at a spacecraft represent a superposition of the inducing (primary) and the induced components. There is a large interest in knowing both the inducing and the induced components of the field as accurate as possible. On the one hand, knowledge about spatio-temporal variability of the inducing field constrains the state of source currents in the ionosphere and the magnetosphere (Yamazaki and Maute, 2017; Balasis and Egbert, 2006; Tsyganenko, 2019), which in turn represents a crucial input for accurate geomagnetic field modelling (Maus and Weidelt, 2004; Finlay et al, 2017) and space weather hazard evaluation (Pulkkinen et al, 2003; Kelbert, 2020; Juusola et al, 2020). On the other hand, relation between the inducing and the induced field variations, governed by Maxwell's equations, can be used to probe the electrical conductivity distribution in the Earth's subsurface (Olsen, 1999a; Kuvshinov and Olsen, 2006; Kelbert et al, 2009). However, separation of the magnetic field into the inducing and the induced components is often non-trivial owing to their non-linear relationship that depends on the 3-D distribution of electrical conductivity in the Earth's interior. The goal here is to elaborate on this problem further.

To keep the study concise and focused, we make several assumptions that are implied in the derivations and discussions that follow. First, we concentrate on time-variations with periods longer than a few hours, which is beyond the band where a simple plane-wave source assumption is valid (this assumption can be used to model external source fields (Kelbert and Lucas, 2020) and used in the magnetotelluric method (Chave and Jones, 2012) for probing the subsurface electrical conductivity). Second, we assume that field variations are due to the extraneous electric currents and the corresponding electromagnetic response from the conductive Earth's mantle. In other words, the contributions from all other magnetic field sources, such as the crust or the core, are absent in the data (this is never true in practice, but these problems are beyond the scope of our study). Further, the extraneous electric currents are assumed to have their origin in the ionosphere and magnetosphere. By this, we exclude the ocean-induced electromagnetic fields, which require dedicated modelling and inversion approaches (Velímský et al, 2018).

In the most general form, the extraneous source structure needs to be parameterized with spatially heterogeneous functions and estimated from the data along with the subsurface electrical conductivity distribution by solving a corresponding inverse problem. However, joint estimation

of conductivity and external field structures represents a notoriously difficult task. Alternative methods have thus been used to approach the same problem.

Conventionally, the Gauss method has been used to separate the magnetic field into time-series of spherical harmonic (SH) coefficients of internal and external origins (Backus et al, 1996). By relating the internal and the external SH coefficients, one can estimate a transfer function between them and perform the inversion in terms of subsurface electrical conductivity (Olsen, 1999a; Schmucker, 1999; Kuvshinov, 2012) or fit the time-series of SH coefficients directly (Velímský and Knopp, 2021). However, this approach is only applicable to potential fields where inducing field contribution is external to the observer. Moreover, due to sparse measurements, one is typically limited to using a small set of spherical harmonics to describe the inducing and induced parts of the field (Kuvshinov et al, 2021; Velímský and Knopp, 2021).

Recognizing these limitations, a number of recent studies (Koch and Kuvshinov, 2013; Sun et al, 2015; Guzavina et al, 2019; Egbert et al, 2021; Zhang et al, 2022) have adopted an alternative strategy where the source structure is estimated given some prior knowledge about the subsurface conductivity. With this estimated source structure, the inversion in terms of subsurface conductivity is subsequently performed and the updated conductivity model can in turn be used to re-estimate the source coefficients. This approach allows for a more general ansatz to describe the source geometry (Zenhäusern et al, 2021; Egbert et al, 2021; Grayver et al, 2021) and enables derivation of alternative families of transfer functions (Püthe and Kuvshinov, 2014; Guzavina et al, 2019), which are not limited to the potential field assumption. Additionally, one is able to incorporate the prior knowledge on the induction effects due to the ocean and marine sediments (Grayver et al, 2021). Therefore, determination of the inducing source field and the mantle conductivity is performed in an alternating manner on the two separate model spaces (hereinafter termed "alternating approach"). Such separate estimation of the two model spaces is assumed to result in progressively refined knowledge of both the source and the conductivity models.

In this thesis, this idea is developed further and the problem is posed in a form that allows us to simultaneously estimate the source and the subsurface conductivity directly from the data. Since the model space consists of one part (i.e. inducing source currents), upon which the dependence of the observable is linear, and another part (i.e. subsurface electrical conductivity), which enters the objective in a non-linear manner, the underlying inverse problem (under squared loss) falls into the category of a special optimization task known as Separable Nonlinear Least Squares (SNLS) problem.

It will be shown in this thesis that the naive "alternating approach" described above is the simplest way of solving the SNLS problem, although it may lack consistency and suffer from a limited convergence. There exist more efficient ways of solving the SNLS problem. In particular, the variable projection method (hereafter referred to as VP) has been proposed as an optimal method for solving SNLS problems that benefits from both computational efficiency and fast convergence (Golub and Pereyra, 1973, 2003). In essence, VP exploits the linear dependency in one part of the model and estimates this part via linear least squares at each iteration, thus effectively projecting the complete model space onto a reduced subspace for efficient non-linear optimization.

The advantage of variable projection naturally appeals to a number of geophysical inverse problems where the unknown parameters intrinsically constitute separable least squares. Such behaviour is typical of seismic wave propagation and electromagnetic induction, where source characterization is linearly filtered by a medium response, depending non-linearly on medium properties. In the last decade, this algorithm has been recognized in seismology as an efficient way to invert for velocity structure while simultaneously characterizing the source (Rickett, 2013; De Ridder and Maddison, 2018), the source-related calibration parameters (Li et al, 2013), or both the source and the receiver factors (Hu et al, 2021). Despite an early conceptualization (Fainberg et al, 1990), this method, to our knowledge, has not yet been well elaborated in the context of electromagnetic induction problems, where the merit of VP is potentially much more pronounced: the full model inversion including the source and conductivity, which is prohibitive due to high dimensionality and non-linearity, becomes tractable in light of linear variable projection. Here an application of VP to a problem of electromagnetic induction sounding is presented. Through the experiments that follow, it is demonstrated that not only does this approach enable simultaneous estimation of the inducing field structure and the electrical conductivity by using a natural physical link between them, but it also provides insights into the interplay between determination of inducing field and conductivity models in a consistent fashion.

2. Methods

Electromagnetic (EM) field variations are governed by Maxwell's equations, which in the frequency domain read

$$\begin{aligned} \nabla \times \mathbf{E} &= -i\omega \mathbf{B}, \\ \frac{1}{\mu_0} \nabla \times \mathbf{B} &= \sigma \mathbf{E} + \mathbf{j}, \end{aligned} \tag{2.1}$$

where $\sigma(\mathbf{r}) \in \mathbb{R}$ denotes electrical conductivity of medium, $\mathbf{B}(\mathbf{r}, \omega; \sigma)$ and $\mathbf{E}(\mathbf{r}, \omega; \sigma)$ the magnetic and electric fields, respectively, ω the angular frequency and $\mathbf{r}$ the position vector. $\mathbf{j}(\mathbf{r}, \omega)$ gives the density of the extraneous (impressed) currents, which are assumed to originate within the ionosphere and magnetosphere, separated from the solid Earth by a layer of insulating air. We take $\mu = \mu_0$ and $\varepsilon = \varepsilon_0$ for the magnetic permeability and electric permittivity, respectively, and neglect the displacement current since $\omega\varepsilon_0 \ll \sigma$ for the frequency band of interest. Here we adopt the following convention for the Fourier transform

$$\begin{aligned} X(\omega) &= \mathscr{F}[x(t)] = \frac{1}{\sqrt{2\pi}} \int_{-\infty}^{+\infty} x(t) e^{-i\omega t}\, dt, \\ x(t) &= \mathscr{F}^{-1}[X(\omega)] = \frac{1}{\sqrt{2\pi}} \int_{-\infty}^{+\infty} X(\omega) e^{+i\omega t}\, d\omega. \end{aligned} \tag{2.2}$$

The system of Maxwell's equations (2.1) is linear with respect to the current density term $\mathbf{j}$. Thus, the magnetic field due to an arbitrary distribution of the current density can be formally expressed as

$$\mathbf{B}(\mathbf{r}, \omega; \sigma) = \int_{\Omega} \mathbf{G}(\mathbf{r}, \mathbf{r}', \omega; \sigma) \cdot \mathbf{j}(\mathbf{r}', \omega)\, d\mathbf{r}', \tag{2.3}$$

where $\mathbf{G}$ is the Green's tensor of the medium and Ω is the volume occupied by the extraneous currents. A corresponding time-domain counterpart contains a temporal convolution, and has the form

$$\mathbf{B}(\mathbf{r}, t; \sigma) = \int_{-\infty}^{\infty} \int_{\Omega} \mathbf{G}(\mathbf{r}, \mathbf{r}', t - t'; \sigma) \cdot \mathbf{j}(\mathbf{r}', t')\, d\mathbf{r}'\, dt'. \tag{2.4}$$

Eqs. 2.3-2.4 show that the magnetic field is related to the source by a linear operator, which is a non-linear functional of the electrical conductivity. The equivalent for the electric field is straightforward, but is omitted because only magnetic field observations are considered in this study. The forward modelling can thus be expressed in a concise algebraic form

$$\mathbf{d}^{\mathrm{mod}}(\sigma, \mathbf{c}) = \mathbf{F}(\sigma)\, \mathbf{c}, \tag{2.5}$$

where $\mathbf{d}^{\mathrm{mod}}$ is the modelled data vector, $\mathbf{c}$ is an inducing source vector, and $\mathbf{F}(\sigma)$ is a functional of σ that links the field to the extraneous currents. The specific form of $\mathbf{F}(\sigma)$ depends on the specific discretization and parameterization of σ and $\mathbf{j}$, but the general algebraic form accommodates a whole set of modelling approaches, among which the forward modellings described by Eqs. 2.3 and 2.4 are just two specific implementations. Instead of estimating only the electrical conductivity $\sigma(\mathbf{r})$, as is often the case in EM induction sounding, our goal is to simultaneously estimate the unknown variables consisting of both $\sigma(\mathbf{r})$ and extraneous currents $\mathbf{c}$ from observations of the magnetic field taken at specified locations and times. To achieve this goal, we seek the combination of $\sigma(\mathbf{r})$ and $\mathbf{c}$ that minimizes the data misfit

$$\chi^2 = d\left(\mathbf{d}^{\mathrm{obs}}, \mathbf{d}^{\mathrm{mod}}(\sigma, \mathbf{c})\right) = d\left(\mathbf{d}^{\mathrm{obs}}, \mathbf{F}(\sigma)\,\mathbf{c}\right), \tag{2.6}$$

where $\mathbf{d}^{\mathrm{obs}}$ is the observational data vector, constituted by magnetic field observations, and $d(\cdot,\cdot)$ denotes the distance metric on the corresponding Hilbert space. A popular choice for such metric in EM induction soundings is the distance induced by the vector norm inversely weighted by the data covariance,

$$\chi^2 = \frac{1}{2}\left(\mathbf{d}^{\mathrm{obs}} - \mathbf{d}^{\mathrm{mod}}\right)^H \mathbf{C}_d^{-1}\left(\mathbf{d}^{\mathrm{obs}} - \mathbf{d}^{\mathrm{mod}}\right) = \frac{1}{2}\left(\mathbf{d}^{\mathrm{obs}} - \mathbf{F}(\sigma)\,\mathbf{c}\right)^H \mathbf{C}_d^{-1}\left(\mathbf{d}^{\mathrm{obs}} - \mathbf{F}(\sigma)\,\mathbf{c}\right), \tag{2.7}$$

where $\mathbf{C}_d$ is the data covariance matrix. The superscript H denotes the Hermitian transpose of the matrix or vector, as the data vector may be complex. In absence of co-variances, the data samples are assumed to be mutually independent, in which case $\mathbf{C}_d = \mathrm{diag}\left(s_i^2\right)$, where s_i^2 is the variance of the i-th data. Introducing $\mathbf{W} = \mathbf{C}_d^{-1/2} = \mathrm{diag}(s_i^{-1})$, the data misfit can be rewritten as the squared L^2 norm of the weighted residual

$$\chi^2 = \frac{1}{2}\left\|\mathbf{r}_w\right\|_2^2 = \frac{1}{2}\left\|\mathbf{W}\mathbf{r}\right\| = \frac{1}{2}\left\|\mathbf{W}\left(\mathbf{d}^{\mathrm{obs}} - \mathbf{F}(\sigma)\,\mathbf{c}\right)\right\|_2^2 = \frac{1}{2}\left\|\mathbf{d}_w^{\mathrm{obs}} - \mathbf{F}_w(\sigma)\,\mathbf{c}\right\|_2^2. \tag{2.8}$$

Here, $\|\cdot\|_2$ denotes the L^2 norm, $\mathbf{r} = \mathbf{d}^{\mathrm{obs}} - \mathbf{F}(\sigma)\mathbf{c}$ is the residual vector, $\mathbf{r}_w = \mathbf{W}\mathbf{r}$, $\mathbf{d}_w = \mathbf{W}\mathbf{d}$ and $\mathbf{F}_w = \mathbf{W}\mathbf{F}$ are the weighted forms of the residual, the data vector and the linear operator, respectively. Hereinafter we shall drop the superscript of the observational data vector and write $\mathbf{d} = \mathbf{d}^{\mathrm{obs}}$ for brevity. To mitigate the inherent non-uniqueness of the problem, a regularization term $\lambda L(\sigma)$ is added to the objective function, where $L(\cdot)$ is the penalty function, and λ is the regularization strength. Here we consider the penalty function that penalizes the L^2 norm of model complexity, given by $L(\sigma) = \frac{1}{2}\|\mathbf{\Gamma}\sigma\|_2^2$, where $\mathbf{\Gamma}$ is known as the Tikhonov matrix. The

full optimization problem is then given by

$$\min_{\sigma,\mathbf{c}} \frac{1}{2} \|\mathbf{d}_w - \mathbf{F}_w(\sigma)\,\mathbf{c}\|_2^2 + \frac{\lambda}{2}\|\mathbf{\Gamma}\sigma\|_2^2. \tag{2.9}$$

2.1. Joint model space inversion

A naive way to tackle the problem (2.9) is to consider optimization in the joint model space. The model is then stated as a concatenated vector $\mathbf{m} = [\boldsymbol{\sigma}^T, \mathbf{c}^T]^T$. Adopting the notations in Hong et al (2017), the Jacobian of the misfit term (Eq. 2.8) is correspondingly given as

$$\mathbf{J}_m = [\mathbf{J}_\sigma, \mathbf{J}_c], \tag{2.10}$$

where $\mathbf{J}_\sigma$ and $\mathbf{J}_c$ are the partial derivatives defined as

$$\begin{aligned} \mathbf{J}_c &= \frac{\partial \mathbf{r}_w}{\partial \mathbf{c}} = -\mathbf{F}_w(\sigma), \\ \mathbf{J}_\sigma &= \frac{\partial \mathbf{r}_w}{\partial \sigma} = -\mathsf{D}\mathbf{F}_w(\sigma)\,\mathbf{c} = \mathsf{D}\mathbf{J}_c\,\mathbf{c}. \end{aligned} \tag{2.11}$$

In what follows, $\mathsf{D}\mathbf{A}$ is used to denote the derivative of $\mathbf{A}$ with respect to σ, where $\mathbf{A}$ is a functional of σ. In its discrete form where $\mathbf{A} \in \mathbb{C}^{i_1 \times i_2 \times \cdots i_l}$, the result $\mathsf{D}\mathbf{A}$ is a tensor of order $l+1$, and the last dimension gives the differentiation component. More explicitly,

$$(\mathsf{D}\mathbf{A}(\mathbf{x}))_{i_1 i_2 \cdots i_{l+1}} = \frac{\partial A_{i_1 i_2 \cdots i_l}}{\partial x_{i_{l+1}}}. \tag{2.12}$$

For $l \geq 2$, matrix multiplications involving $\mathsf{D}\mathbf{A}$ are always assumed to be performed on the leading 2 dimensions. In Gauss-Newton algorithm, the Hessian (i.e. the second order derivative) of the data misfit can be approximated using only the Jacobian of the residual vector

$$\mathbf{H}_m \approx \mathbf{J}_m^H \mathbf{J}_m = \begin{bmatrix} \mathbf{J}_\sigma^H \mathbf{J}_\sigma & \mathbf{J}_\sigma^H \mathbf{J}_c \\ \mathbf{J}_c^H \mathbf{J}_\sigma & \mathbf{J}_c^H \mathbf{J}_c \end{bmatrix}. \tag{2.13}$$

Adding the regularization term, we come up with the model update for the joint model space, which is given by the linear system

$$\begin{bmatrix} \mathbf{J}_\sigma^H \mathbf{J}_\sigma + \lambda \mathbf{\Gamma}^T \mathbf{\Gamma} & \mathbf{J}_\sigma^H \mathbf{J}_c \\ \mathbf{J}_c^H \mathbf{J}_\sigma & \mathbf{J}_c^H \mathbf{J}_c \end{bmatrix} \begin{bmatrix} \Delta\sigma \\ \Delta\mathbf{c} \end{bmatrix} = - \begin{bmatrix} \mathbf{J}_\sigma^H \mathbf{r}_w \\ \mathbf{J}_c^H \mathbf{r}_w \end{bmatrix}. \tag{2.14}$$

The linear system has a total dimension of $M_\sigma + M_c$, where M_σ and M_c are the dimensions of the models σ and $\mathbf{c}$, respectively. In geomagnetic deep sounding problems the inducing field parameterization usually occupies much higher dimensions than the conductivity model due to its temporal dependency, i.e. $M_c \gg M_\sigma$. Seeking a solution to the stated problem directly in the joint model space hence induces a fully non-linear optimization in a high-dimensional space, a problem formidable to tackle. Using Schur complement, however, it is possible to formally separate the solved model updates of system 2.14 into the updates on separate models. Invoking the invertibility of $\mathbf{J}_c^H \mathbf{J}_c$, the model update on σ is formally given by

$$\left[\mathrm{Re}\left[\mathbf{J}_\sigma^H \left(\mathbf{I} - \mathbf{J}_c \mathbf{J}_c^\dagger\right) \mathbf{J}_\sigma\right] + \lambda \Gamma^T \Gamma\right] \Delta\sigma = -\mathrm{Re}\left[\mathbf{J}_\sigma^H \left(\mathbf{I} - \mathbf{J}_c \mathbf{J}_c^\dagger\right) \mathbf{r}_w\right], \tag{2.15}$$

where $\mathbf{A}^\dagger$ denotes the Moore-Penrose pseudoinverse of matrix $\mathbf{A}$. The real parts of the Hessian and the gradient are taken to enforce real update on σ. After $\Delta\sigma$ is solved, the model $\mathbf{c}$ is similarly updated at each iteration via

$$\left[\mathbf{J}_c^H \mathbf{J}_c\right] \Delta\mathbf{c} = -\mathbf{J}_c^H \left(\mathbf{r}_w + \mathbf{J}_\sigma \Delta\sigma\right). \tag{2.16}$$

The invertibility of $\mathbf{J}_c^H \mathbf{J}_c$ is a well justified assumption in the context of geomagnetic field estimation. As the equation $\mathbf{J}_c\, \mathbf{c} \simeq -\mathbf{d}_w$ gives the linear system for estimating the inducing source currents, the conditioning of $\mathbf{J}_c^H \mathbf{J}_c$ is associated with the well-posedness of the inducing source estimation. In practice, the problem of inducing source estimation is usually a well-posed problem providing adequate observational coverage and appropriate source paramterization, and so hereinafter we shall always assume that $\mathbf{J}_c^H \mathbf{J}_c = \mathbf{F}_w^H(\sigma)\mathbf{F}_w(\sigma)$ is invertible, and the pseudoinverse can be explicitly written as $\mathbf{J}_c^\dagger = (\mathbf{J}_c^H \mathbf{J}_c)^{-1} \mathbf{J}_c^H$.

2.2. Variable projection approach

As already mentioned, the magnetic field data is a linear functional of the extraneous currents parameterized as $\mathbf{c}$, but a non-linear functional of the medium electrical conductivity $\sigma(\mathbf{r})$. This particular structure of the inverse problem with data misfit defined in Eq. 2.8 makes it an example of the so-called separable non-linear least squares (SNLS) and allows us to adopt more efficient methods to solve it.

Variable projection has been first proposed by Golub and Pereyra (1973) as an optimization method for solving SNLS problems. Exploiting the linear dependency on $\mathbf{c}$, at each given conductivity model $\hat{\sigma}$, the best-fitting linear part can be obtained via a linear regression $\hat{\mathbf{c}} =$

$\mathbf{F}_w^\dagger(\hat{\sigma})\,\mathbf{d}_w$. With the linear regression at each iteration, the optimization is then effectively "constrained" to a reduced, nonlinear model space

$$\begin{aligned}
&\min_\sigma \frac{1}{2}\,\|\mathbf{d}_w - \mathbf{F}_w(\sigma)\,\hat{\mathbf{c}}(\sigma)\|_2^2 + \frac{\lambda}{2}\|\mathbf{\Gamma}\sigma\|_2^2 \\
=&\min_\sigma \frac{1}{2}\left\|\mathbf{d}_w - \mathbf{F}_w(\sigma)\,\mathbf{F}_w^\dagger(\sigma)\,\mathbf{d}_w\right\|_2^2 + \frac{\lambda}{2}\|\mathbf{\Gamma}\sigma\|_2^2 \\
=&\min_\sigma \frac{1}{2}\left\|\mathbf{P}^\perp_{\mathbf{F}_w}(\sigma)\,\mathbf{d}_w\right\|_2^2 + \frac{\lambda}{2}\|\mathbf{\Gamma}\sigma\|_2^2,
\end{aligned} \tag{2.17}$$

where $\mathbf{P}^\perp_{\mathbf{F}_w} = \mathbf{I} - \mathbf{F}_w\mathbf{F}_w^\dagger$ is the projector onto the orthogonal complement of the range of $\mathbf{F}_w(\sigma)$.

The minimum to the non-linear optimization problem in Eq. 2.17 can be found by using either a gradient-based or a Newton-based optimization method. In these cases, the update on the nonlinear model involves evaluation of the Fréchet derivatives with respect to the nonlinear parameters. In turn, this requires us to incorporate the implicit dependency of $\mathbf{c}$ on σ. Golub and Pereyra (1973) derived the expressions for the gradient of the objective function and the Jacobian of the residual vector in terms of pseudoinverses and derivatives of the linear operator $\mathbf{F}_w$. With the notations defined in Eq. 2.12, the linear projection can also be stated as $\hat{\mathbf{c}} = -\mathbf{J}_c^\dagger\,\mathbf{d}_w$, and the orthogonal projector is given by $\mathbf{P}^\perp_{\mathbf{F}_w} = \mathbf{I} - \mathbf{J}_c\mathbf{J}_c^\dagger = \mathbf{P}^\perp_{\mathbf{J}_c}$. Note that the two explicit Jacobians are coupled in model space (i.e. $\mathbf{J}_\sigma$ and $\mathbf{J}_c$ are dependent upon $\mathbf{c}$ and σ, respectively). This will be clearly seen in the case of variable projection, where the complete Jacobian of the misfit term reformulated with variable projection (Eq. 2.17) is given by

$$\mathbf{J}(\sigma, \hat{\mathbf{c}}(\sigma)) = \mathsf{D}\mathbf{r}_w = \mathbf{J}_\sigma + \mathbf{J}_c\,\mathsf{D}\hat{\mathbf{c}} = \mathbf{J}_\sigma - \mathbf{J}_c\,\mathsf{D}\mathbf{J}_c^\dagger\,\mathbf{d}_w. \tag{2.18}$$

Invoking the derivative of pseudoinverse (see Golub and Pereyra 1973 for derivation details),

$$\mathsf{D}\mathbf{A}^\dagger = -\mathbf{A}^\dagger\,\mathsf{D}\mathbf{A}\,\mathbf{A}^\dagger + \mathbf{A}^\dagger\left(\mathbf{A}^\dagger\right)^H(\mathsf{D}\mathbf{A})^H\,\mathbf{P}^\perp_{\mathbf{A}} + \left(\mathbf{P}^\perp_{\mathbf{A}^H}\right)^H(\mathsf{D}\mathbf{A})^H\left(\mathbf{A}^\dagger\right)^H\mathbf{A}^\dagger, \tag{2.19}$$

the complete Jacobian of the variable-projected system can hence be reiterated and expressed solely in terms of $\mathbf{J}_\sigma$, $\mathbf{J}_c$ together with its derivative and pseudoinverse

$$\begin{aligned}
\mathbf{J}(\sigma, \hat{\mathbf{c}}(\sigma)) &= \mathbf{J}_\sigma - \mathbf{J}_c\left(-\mathbf{J}_c^\dagger\,\mathsf{D}\mathbf{J}_c\,\mathbf{J}_c^\dagger + \mathbf{J}_\mathbf{c}{}^\dagger(\mathbf{J}_\mathbf{c}{}^\dagger)^H(\mathsf{D}\mathbf{J}_\mathbf{c})^H\mathbf{P}^\perp_{\mathbf{J}_c} + \left(\mathbf{P}^\perp_{\mathbf{J}_c^H}\right)^H(\mathsf{D}\mathbf{J}_c)^H(\mathbf{J}_c^\dagger)^H\mathbf{J}_\mathbf{c}{}^\dagger\right)\mathbf{d}_w \\
&= \mathbf{J}_\sigma - \mathbf{J}_c\mathbf{J}_\mathbf{c}{}^\dagger\,\mathsf{D}\mathbf{J}_c\,\hat{\mathbf{c}} - \mathbf{J}_\mathbf{c}\mathbf{J}_\mathbf{c}{}^\dagger(\mathbf{J}_\mathbf{c}{}^\dagger)^H(\mathsf{D}\mathbf{J}_\mathbf{c})^H\mathbf{P}^\perp_{\mathbf{J}_\mathbf{c}}\mathbf{d}_w + \mathbf{J}_c\left(\mathbf{P}^\perp_{\mathbf{J}_c^H}\right)^H(\mathsf{D}\mathbf{J}_c)^H(\mathbf{J}_\mathbf{c}{}^\dagger)^H\hat{\mathbf{c}} \\
&= \mathbf{J}_\sigma - \mathbf{J}_c\mathbf{J}_c^\dagger\mathbf{J}_\sigma - \left(\mathbf{J}_c^\dagger\right)^H(\mathsf{D}\mathbf{J}_c)^H\,\mathbf{P}^\perp_{\mathbf{J}_c}\mathbf{d}_w.
\end{aligned} \tag{2.20}$$

The last step uses the fact that $\mathbf{A}\mathbf{A}^\dagger(\mathbf{A}^\dagger)^H = \left(\mathbf{A}\mathbf{A}^\dagger\right)^H(\mathbf{A}^\dagger)^H = \left(\mathbf{A}^\dagger\mathbf{A}\mathbf{A}^\dagger\right)^H = \left(\mathbf{A}^\dagger\right)^H$ and

$\mathbf{A}\left(\mathbf{P}^{\perp}_{\mathbf{A}^H}\right)^H = \mathbf{A}\left(\mathbf{I}-\mathbf{A}^H(\mathbf{A}^\dagger)^H\right)^H = \mathbf{A}\left(\mathbf{I}-\mathbf{A}^\dagger\mathbf{A}\right) \equiv \mathbf{0}$. Part of the dependency of $\mathbf{c}$ upon σ, namely the 3rd term in Eq. 2.19, has no contribution to the complete Jacobian since it is perpendicular to $\mathbf{J}_c$. Therefore the complete Jacobian is simply

$$\begin{aligned}\mathbf{J}(\sigma,\hat{\mathbf{c}}(\sigma)) &= \mathbf{J}_\sigma - \mathbf{J}_c\mathbf{J}_c^\dagger\mathbf{J}_\sigma - \left(\mathbf{J}_c^\dagger\right)^H(\mathsf{D}\mathbf{J}_c)^H\,\mathbf{P}^{\perp}_{\mathbf{J}_c}\mathbf{d}_w \\ &= \mathbf{J}_\sigma - \mathbf{J}_c\mathbf{J}_c^\dagger\mathbf{J}_\sigma - \left(\mathbf{J}_c^\dagger\right)^H(\mathsf{D}\mathbf{J}_c)^H\,\mathbf{r}_w.\end{aligned} \tag{2.21}$$

Note that if an inverse problem were conducted solely in the space of σ, then only the the first term, namely $\mathbf{J}_\sigma$, would be present. The trailing two terms involve the dependency of the source estimate on the change in subsurface conductivity, confining the model updates of σ to the hyperplane defined by the regression of $\mathbf{c}$. Reintroducing linear operators via Eq. 2.11, we arrive at the expression for the Jacobian of the residual vector

$$\begin{aligned}\mathbf{J} &= \mathbf{P}^{\perp}_{\mathbf{J}_c}\mathbf{J}_c\hat{\mathbf{c}} - \left(\mathbf{P}^{\perp}_{\mathbf{J}_c}\,\mathsf{D}\mathbf{J}_c\mathbf{J}_c^\dagger\right)^H\mathbf{d}_w \\ &= -\mathbf{P}^{\perp}_{\mathbf{F}_w}\,\mathsf{D}\mathbf{F}_w\,\mathbf{F}_w^\dagger\mathbf{d}_w - (\mathbf{P}^{\perp}_{\mathbf{F}_w}\,\mathsf{D}\mathbf{F}_w\,\mathbf{F}_w^\dagger)^H\mathbf{d}_w.\end{aligned} \tag{2.22}$$

Accordingly, the gradient of the misfit function reads

$$\mathrm{grad}\chi^2 = \mathsf{D}\chi^2 = \mathrm{Re}\left[\mathbf{J}^H\mathbf{r}_w\right] = -\mathrm{Re}\left[\left(\mathsf{D}\mathbf{F}_w\,\mathbf{F}_w^\dagger\mathbf{d}_w\right)^H\mathbf{P}^{\perp}_{\mathbf{F}_w}\mathbf{d}_w\right] = \mathrm{Re}\left[\mathbf{J}_\sigma^H\mathbf{r}_w\right]. \tag{2.23}$$

The inversion scheme that calculates Jacobian via Eq. 2.22 is hereinafter referred to as the full-VP scheme. In the case of a 1-D radial conductivity model, the calculation of $\mathsf{D}\mathbf{F}_w$ is cheap and can often be calculated semi-analytically. For a general 3-D conductivity model, the evaluation of $\mathsf{D}\mathbf{F}_w$ is often the resource demanding part of the inversion. Even when the adjoint method (Pankratov and Kuvshinov, 2010; Egbert and Kelbert, 2012) can be used such that each evaluation of the $\mathsf{D}\mathbf{F}_w$ term requires one forward and one adjoint solution for given inducing sources, 3-D electromagnetic modelling itself remains very computationally demanding. It is therefore desirable to explore approximations that allow for fewer evaluations of $\mathsf{D}\mathbf{F}_w$.

Two such approximations have been proposed by Ruhe and Wedin (1980). One option is to drop the last term in Eq. 2.21, effectively dropping the 2nd term in Eq. 2.22, yielding

$$\mathbf{J} = -\mathbf{P}^{\perp}_{\mathbf{F}_w}\,\mathsf{D}\mathbf{F}_w\,\mathbf{F}_w^\dagger\mathbf{d}_w = \mathbf{P}^{\perp}_{\mathbf{F}_w}\mathbf{J}_\sigma. \tag{2.24}$$

We adopt the terminology used by Hong et al (2017) and refer to this as the VP-RW2 scheme. The dropped term contains higher-order derivatives of the residual vector, and is considered a higher-order refinement. This scheme retains high convergence rate and accuracy, while

outperforming the full-VP in terms of computational efficiency (Ruhe and Wedin, 1980; O'Leary and Rust, 2013). The second option is to drop both the 2nd and the 3rd terms in Eq. 2.21, leading to the very simple form

$$\mathbf{J} = -\mathsf{D}\mathbf{F}_w \, \mathbf{F}_w^{\dagger}\mathbf{d}_w = \mathbf{J}_\sigma, \tag{2.25}$$

hereinafter referred to as the VP-RW3 scheme. This is equivalent to assuming fixed inducing currents (i.e. $\mathsf{D}\hat{\mathbf{c}} = 0$) at each iteration while searching for updates on the conductivity structure. This is in contrast to both full-VP and VP-RW2 schemes, where Jacobian contains additional information on the implicit feedback of the source.

Eqs. 2.22, 2.24 and 2.25 define the first order Fréchet derivatives with the variable projection. As can be seen from the derivations, these three variants are closely related in the scope of variable projection but have different levels of approximation. Despite poor performance of the VP-RW3 scheme previously reported by Hong et al (2017) in matrix factorization problems, we chose to consider this scheme here, particularly because of its resemblance to what we call the "alternating approach", which is revisited in the next section under the framework of variable projection.

As alluded to, the VP method plays the role of a surrogate method for joint model space inversion. This connection between the two approaches can be stated more explicitly. To avoid higher order derivatives, we again consider the model update proposed by Gauss-Newton algorithm, where the Hessian is approximated as $\mathbf{H} \approx \mathrm{Re}[\mathbf{J}^H\mathbf{J}]$. The model update can be expressed as

$$\left(\mathrm{Re}\left[\mathbf{J}^H\mathbf{J}\right] + \lambda\boldsymbol{\Gamma}^T\boldsymbol{\Gamma}\right)\, \delta\sigma = -\mathsf{D}\chi^2. \tag{2.26}$$

Plugging in Eqs. 2.22 to 2.25, the model updates take the form

$$\begin{aligned}
\left[\mathrm{Re}\left[\mathbf{J}_\sigma^H\mathbf{P}_{\mathbf{J}_c}^{\perp}\mathbf{J}_\sigma + \mathbf{r}_w^H\mathsf{D}\mathbf{J}_c\left(\mathbf{J}_c^H\mathbf{J}_c\right)^{-1}\mathsf{D}\mathbf{J}_c^H\mathbf{r}_w\right] + \lambda\boldsymbol{\Gamma}^T\boldsymbol{\Gamma}\right]\Delta\sigma &= -\mathrm{Re}\left[\mathbf{J}_\sigma^H\mathbf{r}_w\right] \quad (\mathrm{full}-\mathrm{VP}),\\
\left[\mathrm{Re}\left[\mathbf{J}_\sigma^H\mathbf{P}_{\mathbf{J}_c}^{\perp}\mathbf{J}_\sigma\right] + \lambda\boldsymbol{\Gamma}^T\boldsymbol{\Gamma}\right]\Delta\sigma &= -\mathrm{Re}\left[\mathbf{J}_\sigma^H\mathbf{r}_w\right] \quad (\mathrm{VP}-\mathrm{RW2}),\\
\left[\mathrm{Re}\left[\mathbf{J}_\sigma^H\mathbf{J}_\sigma\right] + \lambda\boldsymbol{\Gamma}^T\boldsymbol{\Gamma}\right]\Delta\sigma &= -\mathrm{Re}\left[\mathbf{J}_\sigma^H\mathbf{r}_w\right] \quad (\mathrm{VP}-\mathrm{RW3}).
\end{aligned} \tag{2.27}$$

Immediately the resemblance between Eq. 2.15 and the VP-RW2 scheme in Eq. 2.27 is noticeable. The two linear systems share the same left-hand-side terms, only differing from each other in the right-hand-side term, i.e. the gradient. In particular, when the current model in the joint model space has the form $\mathbf{m} = [\sigma, \mathbf{c}] = [\sigma, -\mathbf{J}_c^{\dagger}\mathbf{d}_w]$, we will have the orthogonal property of the

residual vector with respect to $\mathbf{J}_c$

$$\mathbf{J}_c^H \mathbf{r}_w = \mathbf{0} \quad \Longrightarrow \quad \left(\mathbf{I} - \mathbf{J}_c \mathbf{J}_c^\dagger\right) \mathbf{r}_w = \mathbf{r}_w. \tag{2.28}$$

The linear system for joint model space optimization (Eq. 2.15) is then effectively the same as VP-RW2 (Eq. 2.27). We therefore conclude that given the same conductivity model σ and an optimized source model $\mathbf{c} = -\mathbf{J}_c^\dagger(\sigma)\,\mathbf{d}_w$, the conductivity model update proposed by VP-RW2 is exactly the same as that proposed by the joint model space inversion. It is, however, worthy of noticing that the proposed linear update in joint model space inversion (Eq. 2.16) does not yield optimized update on $\mathbf{c}$. In contrast, the VP methods conduct regression at every iteration, which guarantees that the choice of $\mathbf{c}$ at current σ is optimal. Therefore, starting from the same $\sigma, \mathbf{c} = -\mathbf{J}_c^\dagger \mathbf{d}_w$ combinations, VP-RW2 is guaranteed to propose a model with a lower misfit, without resorting to more complex conductivity models.

As a final remark, we observe that the gradient $\mathsf{D}\chi^2$ always has the same expression as in Eq. 2.22, regardless of the approximation used for constructing the Jacobian. This is due to the fact that as $\hat{\mathbf{c}} = \mathbf{F}_w^\dagger \mathbf{d}_w$ guarantees that the source parameters minimize the squared misfit of the data, the residual automatically lives in the orthogonal complement of the linear operator, and only manifest itself through $\mathbf{J}_\sigma$. In other words, as long as the current source estimation minimizes the data misfit, gradients do not sense the implicit feedback of the source, but always view the source as if it were a fixed ground truth, as has been noticed by Aravkin and Leeuwen (2012). Therefore, purely gradient-based optimization schemes are not affected by the choice of the variant of VP. Optimization schemes utilizing higher order information, such as Gauss-Newton algorithm and Levenberg-Marquardt algorithms, are however different for different VP variants.

2.3. Alternating approach

The so-called "alternating approach" naturally follows the conventional scenario where community concerned with the magnetospheric/ionospheric current system and the community concerned with mantle electrical conductivity structure conduct research separately based on one anothers' estimates of their respective models, contributing to an iterative refinement of both models. Combining these procedures, Koch and Kuvshinov (2013) proposed a scheme where, starting from an initial model of mantle conductivity, one first comes up with a preliminary estimate of the inducing currents, then recovers the conductivity model based on the estimated source, and then goes back to refining the source with the "recovered" mantle conductivity. In

a very recent work, Zhang et al (2022) utilized the same alternating strategy to invert for the conductivity in the mantle transition zone (MTZ), in combination with a model-based inducing current representation. This procedure can in principle be repeated several times, until the model estimates or the data misfits reach certain convergence criteria.

Similar to variants of the variable projection, the alternating approach also offers a way to optimize on external currents and mantle conductivity simultaneously, without resorting to fully non-linear inversion. It can be viewed as a conglomeration of successive inversions, conventionally carried out separately, with respect to external currents and mantle conductivity. The major difference from VP is that in the case of a naive alternating approach, once one part of the model is estimated, inversion on the other part is carried out in a complete standalone stage to minimize the objective. This difference is especially pronounced during inversion of the electrical conductivity, where a significant number of iterations are usually needed to capture the non-linear dependence of the predicted data on the conductivity model. In VP, estimate on the source is projected and updated at each iteration step and is only used for one update, while in the alternating approach, all iterations on the conductivity model in one inversion phase are conducted under a fixed source. Such approach may potentially lead to high redundancy in iterations, if not deterioration of the model estimates.

In this study we revisit and generalize the idea of alternating approach, by implementing a flexible version of the inversion scheme for our problem. The implementation used here is based on nonlinear model updates: at each iteration, update on the nonlinear model is generated by Gauss-Newton method, while the source is kept fixed. At iterations pre-defined by certain criteria (referred to as the linear update criteria), the inducing source is updated. The scheme can be summarized by the pseudo-code as follows.

$$
\begin{aligned}
&\text{Iteration } k=0: \quad \mathbf{c}^{(0)} = \mathbf{F}_w^{\dagger}(\sigma^{(0)})\mathbf{d}_w \\
&\text{Iteration } k>0: \quad \text{Solve} \quad \left(\mathrm{Re}\left[\mathbf{J}_\sigma^H \mathbf{J}_\sigma\right] + \lambda \boldsymbol{\Gamma}^T\boldsymbol{\Gamma}\right)\Delta\sigma^{(k)} = -\mathsf{D}\chi^2(\sigma^{(k-1)}, \mathbf{c}^{(k-1)}) \\
&\qquad\qquad \Longleftrightarrow \quad \left(\mathrm{Re}[(\mathbf{c}^{(k-1)})^H \mathsf{D}\mathbf{F}_w^H(\sigma^{(k-1)})\mathsf{D}\mathbf{F}_w(\sigma^{(k-1)})\mathbf{c}^{(k-1)}] + \lambda\boldsymbol{\Gamma}^T\boldsymbol{\Gamma}\right)\Delta\sigma^{(k)} \\
&\qquad\qquad\qquad\quad = \mathrm{Re}\left[(\mathbf{c}^{(k-1)})^H \mathsf{D}\mathbf{F}_w^H(\sigma^{(k-1)})\left(\mathbf{d}_w - \mathbf{F}_w(\sigma^{(k-1)})\,\mathbf{c}^{(k-1)}\right)\right] \\
&\qquad\qquad \text{Update} \quad \sigma^{(k)} = \sigma^{(k-1)} + \Delta\sigma^{(k)}. \\
&\qquad\qquad \text{If } k \text{ satisfies linear update criteria,} \\
&\qquad\qquad\qquad \mathbf{c}^{(k)} := \mathbf{F}_w^{\dagger}(\sigma^{(k)})\,\mathbf{d}_w. \\
&\qquad\qquad \text{Else,} \quad \mathbf{c}^{(k)} = \mathbf{c}^{(k-1)}
\end{aligned}
\tag{2.29}
$$

By varying the linear update criterion, this implementation can potentially incorporate a spectrum of inversion schemes. For instance, by disabling update on the linear model until the inversion on the nonlinear part has reached convergence, one obtains one end-member scenario, which is exactly the approach as described in Koch and Kuvshinov (2013). This scenario contains the least frequent linear model estimations. In contrast, by forcing linear model regression at each iteration, one obtains the other end-member, a scheme equivalent to the VP-RW3 (Eq. 2.25). A customized linear update criterion allows gradual change between these two end-members.

2.4. Forward modelling

The coexistence of linear and non-linear model spaces are innate properties of EM induction sounding stemming from the governing Maxwell's equations. Therefore, the formulation provided above is general and will apply to any EM sounding problem where both source and physical properties are unknown. In order to test different inversion approaches, we need to choose a specific form of inducing source parameterization $\mathbf{c}$ and a forward modelling operator $\mathbf{F}(\sigma)$, which is introduced in this section. The experiment in this study is limited to a simple scenario satisfying the following two assumptions. First, we consider only observations made within a current-free space between the inducing source and the induced currents. In other words, the observed magnetic field is potential ($\mathbf{B} = -\nabla V$), where the potential field V can be expanded using Spherical Harmonic (SH) functions in the frequency domain as

$$V(\mathbf{r},\omega) = \sum_{n,m} \left[\varepsilon_n^m(\omega) \left(\frac{r}{a}\right)^n + \iota_n^m(\omega) \left(\frac{r}{a}\right)^{-(n+1)} \right] Y_n^m(\theta,\varphi), \tag{2.30}$$

where $\sum_{n,m} \equiv \sum_{n=1}^{N} \sum_{m=-n}^{n}$; $Y_n^m(\theta,\varphi) = P_n^{|m|}(\theta) e^{\mathrm{i}m\phi}$ is a complex SH function of degree n and order m, with $P_n^{|m|}$ being Schmidt quasi-normalized associated Legendre functions, $\mathbf{r} = (r,\theta,\phi)$ is the position vector in spherical coordinates, and a is the Earth radius; ε_n^m and ι_n^m are the external and internal SH coefficients, respectively.

Second, we assume a 1D radial conductivity structure of the Earth (that is, $\sigma(\mathbf{r}) \equiv \sigma(r)$). This assumption allows us to use a Q-response to describe the induction in the model (Olsen, 1999b). Q-response is a frequency-dependent electromagnetic transfer function (TF) that is independent of the spherical harmonic order m for 1D radially symmetric conductivity, and is formally defined as the ratio of the internal Gauss coefficient to its corresponding external

counterpart

$$Q_n(\omega;\sigma) = \frac{\iota_n^m(\omega;\sigma)}{\varepsilon_n^m(\omega)}. \tag{2.31}$$

With $\iota_n^m(\omega) = Q_n(\omega)\varepsilon_n^m(\omega)$, the forward operator that links magnetic field ($\mathbf{B}$) with model parameters (external coefficients ε and conductivity σ) can be stated as follows

$$\begin{aligned}
B_r(\mathbf{r},\omega) &= -\sum_{n,m}\left[n\left(\frac{r}{a}\right)^{n-1} - (n+1)Q_n(\omega;\sigma)\left(\frac{r}{a}\right)^{-(n+2)}\right] Y_n^m(\theta,\varphi)\,\varepsilon_n^m(\omega),\\
B_\theta(\mathbf{r},\omega) &= -\sum_{n,m}\left[\left(\frac{r}{a}\right)^{n-1} + Q_n(\omega;\sigma)\left(\frac{r}{a}\right)^{-(n+2)}\right] \frac{\partial Y_n^m(\theta,\varphi)}{\partial\theta}\,\varepsilon_n^m(\omega),\\
B_\varphi(\mathbf{r},\omega) &= -\sum_{n,m}\left[\left(\frac{r}{a}\right)^{n-1} + Q_n(\omega;\sigma)\left(\frac{r}{a}\right)^{-(n+2)}\right] \frac{1}{\sin\theta}\frac{\partial Y_n^m(\theta,\varphi)}{\partial\varphi}\,\varepsilon_n^m(\omega).
\end{aligned} \tag{2.32}$$

Eq. 2.32 gives the magnetic field at position $\mathbf{r}$ and at frequency ω in terms of the unknown variables σ and ε_n^m, which can be reformulated in the vector form

$$\mathbf{B}(\mathbf{r},\omega) = \sum_{n,m}\mathbf{B}_n^m(\mathbf{r},\omega;\sigma)\,\varepsilon_n^m(\omega), \tag{2.33}$$

where $\mathbf{B}(\mathbf{r},\omega)\in\mathbb{C}^3$ is the vector magnetic field in the frequency domain, and $\mathbf{B}_n^m(\mathbf{r},\omega;\sigma)\in\mathbb{C}^3$ is the transfer function related to mode ε_n^m for a given $\mathbf{r}$ and ω, whose detailed expression is given in Eq. 2.32. While the SH coefficients ε_n^m in Eq. 2.30 appear to be coefficients of the potential field, they can also be used for representing the inducing current. To this end, consider an extraneous sheet current floating at an altitude h, then the sheet current density can be written as $\mathbf{j}(\mathbf{r},\omega) = -\delta(r-b)\hat{\mathbf{e}}_r\times\nabla_H\boldsymbol{\Psi}^{\text{ext}}(\theta,\phi)$, where $b = a+h$, and the external current stream function can be expanded in SH using ε_n^m as

$$\boldsymbol{\Psi}^{\text{ext}}(\theta,\phi) = -\frac{a}{\mu_0}\sum_{n,m}\frac{2n+1}{n+1}\left(\frac{b}{a}\right)^n Y_n^m(\theta,\phi)\,\varepsilon_n^m(\omega). \tag{2.34}$$

It follows that the coefficients $\varepsilon_n^m(\omega)$ give the parameterization of the inducing currents, and constitute the aforementioned source vector $\mathbf{c}$.

It should be stressed here that forward operators with other parameterizations of source currents, not limited to a potential representation, and a general 3-D conductivity distribution are possible (Grayver et al, 2021) and can be incorporated in the formalism of Section 2.2, but this leads to a rather lengthy and technically cumbersome implementation. Choosing a simplified forward operator here allows us to concentrate on studying the properties of SNLS problem and variable projection method in the context of EM induction problems, which is considered as the

main contribution of this thesis. In addition, this forward operator allows direct comparison between the VP / alternating approaches with the conventional approach where TFs are used for inversion, the details of which are elaborated in Section 2.5.

In order to capture the temporal behaviour of the external field as well as its properties in the frequency domain, the forward operator and the inversion are both established in the windowed Fourier domain, where each window is considered a realization of the source. For a given frequency ω and a time window τ, the magnetic field is related to the source coefficients via

$$\mathbf{d}^{\text{mod}}_{\tau,\omega} = \begin{bmatrix} \mathbf{B}(\mathbf{r}_1,\tau,\omega) \\ \vdots \\ \mathbf{B}(\mathbf{r}_{N_r},\tau,\omega) \end{bmatrix} = \begin{bmatrix} \mathbf{B}^0_1(\mathbf{r}_1,\omega;\sigma) & \cdots & \mathbf{B}^N_N(\mathbf{r}_1,\omega;\sigma) \\ \vdots & \ddots & \vdots \\ \mathbf{B}^0_1(\mathbf{r}_{N_r},\omega;\sigma) & \cdots & \mathbf{B}^N_N(\mathbf{r}_{N_r},\omega;\sigma) \end{bmatrix} \begin{bmatrix} \varepsilon^0_1(\tau,\omega) \\ \vdots \\ \varepsilon^N_N(\tau,\omega) \end{bmatrix} = \mathbf{B}_{\tau,\omega}(\sigma)\,\mathbf{c}_{\tau,\omega}, \tag{2.35}$$

where $\mathbf{d}$ denotes the data vector, $\mathbf{c}$ denotes the vector of external SH coefficients, and the subscripts τ and ω indicate the time window and frequency, respectively. By concatenating time windows and periods, the forward operator with respect to the complete set of observations can be recast to the algebraic form

$$\mathbf{d}^{\text{mod}}_{\omega} = \begin{bmatrix} \mathbf{d}^{\text{mod}}_{\tau_1,\omega} \\ \vdots \\ \mathbf{d}^{\text{mod}}_{\tau_{N_\tau},\omega} \end{bmatrix} = \begin{bmatrix} \mathbf{B}_{\tau_1,\omega}(\sigma) & & \mathbf{0} \\ & \ddots & \\ \mathbf{0} & & \mathbf{B}_{\tau_{N_\tau},\omega}(\sigma) \end{bmatrix} \begin{bmatrix} \mathbf{c}_{\tau_1,\omega} \\ \vdots \\ \mathbf{c}_{\tau_{N_\tau},\omega} \end{bmatrix} = \mathbf{B}_{\omega}(\sigma)\,\mathbf{c}_{\omega}, \tag{2.36}$$

$$\mathbf{d}^{\text{mod}} = \begin{bmatrix} \mathbf{d}^{\text{mod}}_{\omega_1} \\ \vdots \\ \mathbf{d}^{\text{mod}}_{\omega_{N_\omega}} \end{bmatrix} = \begin{bmatrix} \mathbf{B}_{\omega_1}(\sigma) & & \mathbf{0} \\ & \ddots & \\ \mathbf{0} & & \mathbf{B}_{\omega_{N_\tau}}(\sigma) \end{bmatrix} \begin{bmatrix} \mathbf{c}_{\omega_1} \\ \vdots \\ \mathbf{c}_{\omega_{N_\omega}} \end{bmatrix} = \mathbf{F}(\sigma)\,\mathbf{c}, \tag{2.37}$$

which is exactly the form given by Eq. 2.5. Here N_τ is the total number of time windows within a frequency band, and N_ω is the total number of frequency bands. The source vector $\mathbf{c}$ defined in Eq. 2.37 thus contains the spectrum of the inducing field coefficients at N_ω frequencies and its time evolution. As a side remark, the linear operator $\mathbf{F}$ in Eq. 2.37, which is the full forward modelling operator in Eq. 2.8, is an extremely sparse, block-diagonal matrix. This is a desired property of modelling in the windowed Fourier domain, as the field observations within each time window are considered to be independent of the source parameters from other time windows. Calculation of $\mathbf{F}^{\dagger}_{w}$, which is used in the estimation of $\mathbf{c}$ and the evaluation of $\mathbf{J}$, can be implemented efficiently by calculating the pseudoinverses of each diagonal block.

2.5. Transfer function inversion

The Q-response defined in Eq. 2.31 is an example of electromagnetic transfer functions, which describe the Earth's induction response to the source field in the frequency domain. Exploiting the dependence of such TFs on the conductivity structure has proven a useful approach to infer subsurface electrical conductivity, and has given rise to a fruitful route of applications (Olsen, 1999c,b; Kuvshinov and Olsen, 2006; Munch et al, 2020). As a member of such TFs, Q-response can be directly used to invert for Earth electrical conductivity (Olsen, 1999a). This method, which involves spherical harmonic analysis (SHA) and internal/external field separation (a process referred to as the Gauss method), Q-response estimation, and electrical conductivity inversion (referred to as Q inversion), is used as a reference method for comparison in the experiments.

Starting from the time series at observatories, we first estimate the external and internal field SH coefficients. By using the potential field representation of the magnetic field $\mathbf{B} = -\nabla V$ and the SH expansion (Eq. 2.30), the magnetic field observations at one time point (e.g. hourly means for an hour, etc.) yield the following linear system

$$\begin{bmatrix} B_r(\mathbf{r}_1,t) \\ B_\theta(\mathbf{r}_1,t) \\ B_\phi(\mathbf{r}_1,t) \\ \vdots \\ B_r(\mathbf{r}_{N_r},t) \\ B_\theta(\mathbf{r}_{N_r},t) \\ B_\phi(\mathbf{r}_{N_r},t) \end{bmatrix} = \begin{bmatrix} B_r^{10,\mathrm{ext}}(\mathbf{r}_1) & \cdots & B_r^{NN,\mathrm{ext}}(\mathbf{r}_1) & B_r^{10,\mathrm{int}}(\mathbf{r}_1) & \cdots & B_r^{NN,\mathrm{int}}(\mathbf{r}_1) \\ B_\theta^{10,\mathrm{ext}}(\mathbf{r}_1) & \cdots & B_\theta^{NN,\mathrm{ext}}(\mathbf{r}_1) & B_\theta^{10,\mathrm{int}}(\mathbf{r}_1) & \cdots & B_\theta^{NN,\mathrm{int}}(\mathbf{r}_1) \\ B_\phi^{10,\mathrm{ext}}(\mathbf{r}_1) & \cdots & B_\phi^{NN,\mathrm{ext}}(\mathbf{r}_1) & B_\phi^{10,\mathrm{int}}(\mathbf{r}_1) & \cdots & B_\phi^{NN,\mathrm{int}}(\mathbf{r}_1) \\ \vdots & & \vdots & & & \\ B_r^{10,\mathrm{ext}}(\mathbf{r}_{N_r}) & \cdots & B_r^{NN,\mathrm{ext}}(\mathbf{r}_{N_r}) & B_r^{10,\mathrm{int}}(\mathbf{r}_{N_r}) & \cdots & B_r^{NN,\mathrm{int}}(\mathbf{r}_{N_r}) \\ B_\theta^{10,\mathrm{ext}}(\mathbf{r}_{N_r}) & \cdots & B_\theta^{NN,\mathrm{ext}}(\mathbf{r}_{N_r}) & B_\theta^{10,\mathrm{int}}(\mathbf{r}_{N_r}) & \cdots & B_\theta^{NN,\mathrm{int}}(\mathbf{r}_{N_r}) \\ B_\phi^{10,\mathrm{ext}}(\mathbf{r}_{N_r}) & \cdots & B_\phi^{NN,\mathrm{ext}}(\mathbf{r}_{N_r}) & B_\phi^{10,\mathrm{int}}(\mathbf{r}_{N_r}) & \cdots & B_\phi^{NN,\mathrm{int}}(\mathbf{r}_{N_r}) \end{bmatrix} \begin{bmatrix} \varepsilon_1^0(t) \\ \vdots \\ \varepsilon_N^N(t) \\ \iota_1^0(t) \\ \vdots \\ \iota_N^N(t) \end{bmatrix}, \tag{2.38}$$

where the matrix elements are given by

$$\begin{aligned} \begin{bmatrix} B_r^{nm,\mathrm{ext}}(\mathbf{r}) \\ B_\theta^{nm,\mathrm{ext}}(\mathbf{r}) \\ B_\phi^{nm,\mathrm{ext}}(\mathbf{r}) \end{bmatrix} &= -\left(\frac{r}{a}\right)^{n-1} \begin{bmatrix} nY_n^m(\theta,\phi) \\ \frac{\partial}{\partial\theta}Y_n^m(\theta,\phi) \\ \frac{1}{\sin\theta}\frac{\partial}{\partial\phi}Y_n^m(\theta,\phi) \end{bmatrix}, \\ \begin{bmatrix} B_r^{nm,\mathrm{int}}(\mathbf{r}) \\ B_\theta^{nm,\mathrm{int}}(\mathbf{r}) \\ B_\phi^{nm,\mathrm{int}}(\mathbf{r}) \end{bmatrix} &= -\left(\frac{a}{r}\right)^{n+2} \begin{bmatrix} -(n+1)Y_n^m(\theta,\phi) \\ \frac{\partial}{\partial\theta}Y_n^m(\theta,\phi) \\ \frac{1}{\sin\theta}\frac{\partial}{\partial\phi}Y_n^m(\theta,\phi) \end{bmatrix}. \end{aligned} \tag{2.39}$$

Eq. 2.38 relates the external and internal field coefficients to the field observations. Given ade-

quate observations and space coverage at time t and an appropriate choice of truncation degree N, the system is over-determined, and a solution of the field coefficients can be constrained. Solving the system induced by a potential magnetic field for external and internal field coefficients is called the Gauss method. The resulting time series of ε_n^m and ι_n^m can then be used to estimate the TF, via e.g. Eq. 2.31. For robustness, the estimation is usually performed on the windowed spectrum of the time series at certain periods. In the discrete form, the windowed spectral transform of a time series $x(t)$ reads

$$X(\tau,\omega) = \mathscr{F}_{\tau,\omega}\left[x(t)\right] = \frac{1}{\sum_k w_k} \sum_{k\in\{k_\tau\}} w_k x(t_k) e^{-i\omega t_k}, \tag{2.40}$$

where k_τ marks the indices of the data points within a time window, w_k is a weighting coefficient associated with the $k-$th point for a tapering window function to suppress spectral leakage. The leading term $\sum_k w_k$ is a normalization factor, which is adopted so that a monochromatic oscillating signal has its amplitude preserved in the transform. The windowed spectra of ε_n^m and ι_n^m from different time windows then constitute multiple realizations that can be used independently to determine Q_n, yielding the overdetermined linear system

$$\mathcal{I}_{nm}(\omega) = \begin{bmatrix} \iota_n^m(\tau_1,\omega) \\ \iota_n^m(\tau_2,\omega) \\ \vdots \\ \iota_n^m(\tau_{N_\tau},\omega) \end{bmatrix} = Q_n(\omega) \begin{bmatrix} \varepsilon_n^m(\tau_1,\omega) \\ \varepsilon_n^m(\tau_2,\omega) \\ \vdots \\ \varepsilon_n^m(\tau_{N_\tau},\omega) \end{bmatrix} = Q_n(\omega)\,\mathcal{E}_{nm}(\omega)\,, \tag{2.41}$$

where $\mathcal{I}_{nm}(\omega), \mathcal{E}_{nm}(\omega) \in \mathbb{C}^{N_\tau}$ are the windowed spectra at frequency ω of the internal and external field coefficients $\iota_n^m(t)$ and $\varepsilon_n^m(t)$, respectively. This method, sometimes referred to as section-averaging, collects the spectral values from multiple time segments as different realizations, and enhances the robustness of the algorithm to noise contamination. Consequently, the linear systems 2.38 and 2.41 that lead to the transfer function Q are standard linear least squares problems, and can be solved in a number of methods. In the implementation used in this thesis, both the least squares problems induced by Eq. 2.38 and 2.41 are solved using the outlier-robust regression with Huber loss. The uncertainties associated with the estimated $\widehat{Q}_n$ can be estimated from the formal variance

$$[\delta\widehat{Q}_n(\omega)]^2 = \frac{1}{N_\tau - 1} \frac{S^2_{\mathcal{I}|\hat{Q}_n}(\omega)}{\mathcal{E}^H_{nm}(\omega)\mathcal{E}_{nm}(\omega)} = \frac{1}{N_\tau - 1} \frac{\|\mathcal{I}_{nm}(\omega) - \mathcal{E}_{nm}(\omega)\,\widehat{Q}_n(\omega)\|_2^2}{\|\mathcal{E}_{nm}(\omega)\|_2^2}. \tag{2.42}$$

With the estimated spectrum of the transfer function $\widehat{Q}_n(\omega)$ and the associated uncertainty

$\delta\widehat{Q}_n(\omega)$, the final step of Q inversion can be stated as a weighted least squares problem

$$\min_{\sigma} \frac{1}{2}\sum_{n=1}^{N}\sum_{k=1}^{K}\left|\frac{\widehat{Q}_n(\omega_k) - Q_n(\omega_k,\sigma)}{\delta\widehat{Q}_n(\omega_k)}\right|^2 + \frac{\lambda}{2}\|\mathbf{\Gamma}\sigma\|_2^2. \tag{2.43}$$

The multistage TF estimation and inversion approach provides a tractable way to separate contributions from the inducing field and the induction currents. However, the shortcoming is also obvious: it must be possible to estimate the TFs as an intermediate result. This significantly restricts the application of such methods. Q response, for instance, can only be estimated under the assumption that the magnetic field is potential and separable into internal (induced) and external (inducing) parts. While the formulations of VP and alternating approaches can easily accomodate any forward modelling that results in the problem 2.9, including the one that utilizes the Q response (Eq. 2.32) and generic time-domain modellings, the TF inversion approaches mostly only work for specific forward operators.

2.6. Optimization

Both VP/alternating approaches and TF inversions boil down to solving the nonlinear least squares, either defined by the misfit on the data (Eq. 2.9) or the misfit on the TFs (e.g. Eq. 2.43) combined with regularizations. For robust and efficient solution to these optimization problems, the trust-region method is used, along with quadratic models approximated using Gauss-Newton method. The Gauss-Newton method provides a simple way to approximate the second-order derivative of the objective function, i.e. the Hessian, with only first-order information on the residual vector, i.e. the Jacobian of the residual. It has the merit of being efficient in computation, as well as always providing positive-semi-definite approximations of the Hessian. Furthermore, the update direction proposed by Gauss-Newton method is guaranteed to be a descent direction whenever the Jacobian is full rank, although the proposed update stepsize may not yield reduced objective (Nocedal and Wright, 2006). A trust region framework, on the other hand, provides an excellent method to safeguard the model updates in the iteration process. In addition to approximating the nonlinear objective function with a quadratic function, a trust region method sets a region of the domain (usually a region bounded by a hypersphere) where such approximation is reliable, known as the trust region. At each iteration, the optimum of the quadratic approximation within the trust region is sought by solving the trust-region subproblem, and the trust region radius is updated based on the predicted and the actual objective function reduction (Conn et al, 2000). It also has the additional merit that in solving the subproblem, a damping is introduced as in typical Levenberg-Marquardt algorithms, which

allows for handling non-positive-definite Hessians, although this is not a concern when using the Gauss-Newton method.

2.7. Data

Having introduced the methods applied to geomagnetic deep sounding problems, we turn to the datasets used for experimentation. In this thesis, both numerical experiments on the synthetic dataset and inversion on real dataset are conducted. Synthetic experiments provide insights into the reconstruction capabilities and convergence properties of different algorithms, while inversion on the real dataset further verifies the validity of the algorithm, and has implications with respect to the application scenarios. As mentioned, the Gauss method and Q inversion approach is also conducted for comparison purposes.

The original dataset used in this thesis consists of hourly means of the observed magnetic field at 163 observatories shown in Figure 2.1. Synthetic data was generated using a realistic external field, and a two layered mantle electrical conductivity model, following the procedures outlined as follows. First, SHA and regression with robust Huber loss is conducted on the real observational data within the time range 2014-2018, yielding hourly time series of the external and internal coefficients up to degree and order 3. For this, only mid-latitude observatories were used (observatories with geomagnetic latitudes between 5° and 56°). The purpose of this step is to obtain time series of the external field that are representative of the real external current system in terms of spatial and temporal characteristics. Using the estimated external field coefficients and a pre-defined 1D Earth electrical conductivity model, synthetic magnetic field time series at real observatory locations are obtained using Eq. 2.32. In this synthetic test, a simple but realistic two-layered mantle conductivity model is set up following the inversion result from Grayver et al (2017) to first order, with an upper-mantle (surface to 660km depth) electrical conductivity of 1.0×10^{-2} S/m, and a lower-mantle (660km to 2900km depth) electrical conductivity of 1.0 S/m. Finally, the synthetic field observation time series are contaminated with a series of independent and identically distributed Gaussian white noise in order to mimic measurement errors.

Since the implementations of the VP methods and the alternating approach are posed in the frequency domain, the same segment-averaging concept is used to prepare the data vector $\mathbf{d}$. The data vector $\mathbf{d}$ is obtained by transforming the time series of magnetic field observations using the windowed spectral transform with tapering defined in Eq. 2.40. As the problem (2.9) is posed in weighted least squares, the weights associated with the observational data play an important role

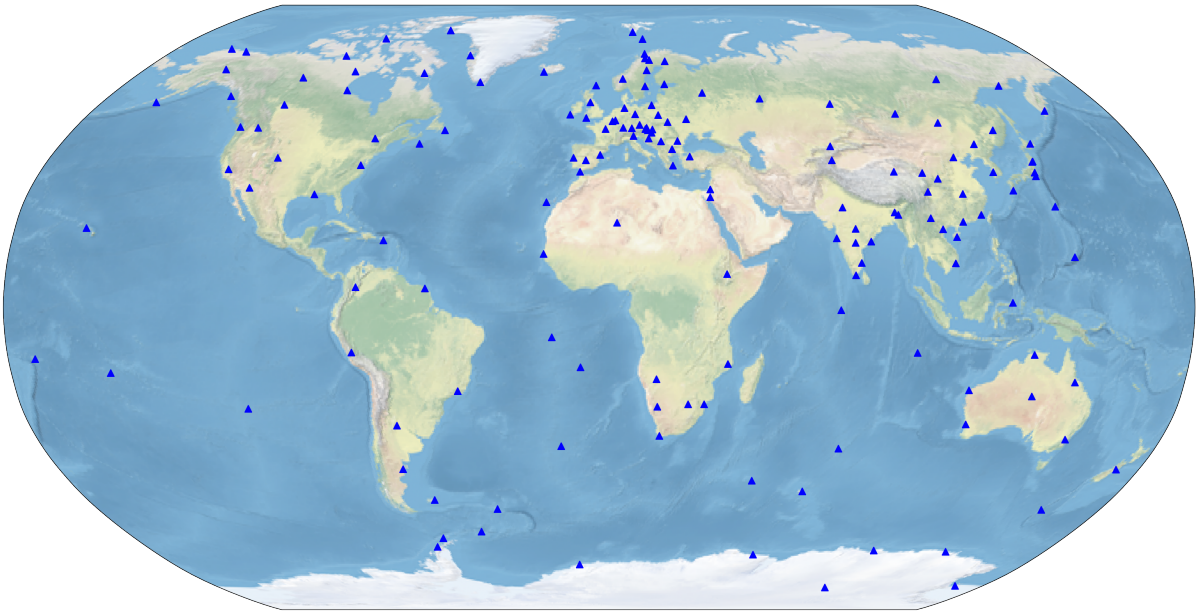

Figure 2.1.: Locations of observatories used in the study. Note that observatories poleward of 55° geomagnetic latitude were excluded.

in the inversion process. In other words, a reasonable estimate of the uncertainties associated with the data is desired. While the uncertainties of the field observations in the time domain may be reasonably estimated, propagating such uncertainties into the windowed Fourier domain requires special attention. For this purpose we consider a time series consisting of a true signal and a random noise

$$x(t_k) = x^{(0)}(t_k) + x'(t_k), \tag{2.44}$$

where $x^{(0)}$ is the signal and x' is the random noise. We assume the noise time series consists of independent and identically distributed (i.i.d.) random variables at each time step, each following the same zero-centered normal distribution, i.e. $x'(t_k) \sim \mathcal{N}(0, s^2)$. The resulting time series $(x'(t_k))$ is then a Gaussian white noise. Invoking linearity of the transform (2.40) with respect to $x(t)$ and the fact that $x(t)$ has a definite spectrum with zero variance, it is self-evident that the variance of $x(t)$ in the windowed Fourier domain is the variance of the defined noise signal,

$$\mathrm{Var}[X(\tau,\omega)] = \mathrm{Var}\left[X'(\tau,\omega)\right] = \mathbb{E}\left[|X'(\tau,\omega)|^2\right] - \left|\mathbb{E}\left[X'(\tau,\omega)\right]\right|^2, \tag{2.45}$$

where $X'(\tau,\omega)$ denotes the windowed spectral transform of $x'(t)$. Inserting the expression of

$X'(\tau,\omega)$ in terms of $x(t_n)$ via Eq. 2.40 we come to the expressions

$$\begin{aligned}
\mathbb{E}\left[X'(\tau,\omega)\right] &= \mathbb{E}\left[\frac{1}{\sum_k w_k}\sum_{k\in\{k_\tau\}} w_k\, x'(t_k)e^{-i\omega t_k}\right] \\
&= \frac{1}{\sum_k w_k}\sum_{k\in\{k_\tau\}} w_k\, \mathbb{E}[x'(t_k)]e^{-i\omega t_k} = 0, \\
\mathbb{E}\left[|X'(\tau,\omega)|^2\right] &= = \mathbb{E}\left[\frac{1}{\left(\sum_k w_k\right)^2}\sum_{k\in\{k_\tau\}}\sum_{l\in\{l_\tau\}} w_k w_l\, \overline{x'(t_k)}x'(t_l)e^{i\omega(t_k-t_l)}\right] \\
&= \frac{1}{\left(\sum_k w_k\right)^2}\sum_{k\in\{k_\tau\}}\sum_{l\in\{l_\tau\}} w_k w_l\, \mathbb{E}\left[\overline{x'(t_k)}x'(t_l)\right] e^{i\omega(t_k-t_l)} \\
&= \frac{1}{\left(\sum_k w_k\right)^2}\sum_{k\in\{k_\tau\}}\sum_{l\in\{l_\tau\}} w_k w_l\, \left(s^2\delta_{kl}\right) e^{i\omega(t_k-t_l)} = \frac{\sum_k w_k^2}{\left(\sum_k w_k\right)^2}s^2.
\end{aligned} \tag{2.46}$$

Here $\overline{x'}$ denotes the complex conjugate of x', and δ_{kl} is the Kronecker delta. The final steps for $\mathbb{E}[X']$ and $\mathbb{E}[|X'|^2]$ use the zero centered property of $x'(t_n)$ and the mutual independence between the values in the time series, respectively. The variance associated with the windowed spectrum is then given by

$$\mathrm{Var}\left[X(\tau,\omega)\right] = \frac{\sum_k w_k^2}{\left(\sum_k w_k\right)^2}s^2. \tag{2.47}$$

Therefore, the spectral uncertainty is not merely proportional to its temporal counterpart, but is also related to the length of the time window. Counter-intuitive as it seems, the uncertainty is roughly inversely proportional to the length of the time window. Longer time windows which stack more temporal measurements into one frequency-domain value lead to lower uncertainties. As Eq. 2.47 is used to estimate the spectral uncertainty in both our synthetic tests and the real data test, due to the aforementioned stacking effect, longer periods are consistently associated with smaller spectral uncertainties, since they require longer time windows. It however needs to be stressed here that Eq. 2.47 is based on the underlying assumption of a Gaussian white noise. This assumption is clearly overly ideal due to long-term drift and other inconsistencies in very long period components of the observations. For the synthetic dataset, however, as the noise added to the synthetic data indeed satisfy the assumption, such estimation of the uncertainty in the frequency domain is optimal.

3. Results

In this study, both synthetic and real data experiments are carried out. In both cases, the VP/alternating methods are tested, along with a conventional approach for field separation and subsurface conductivity inversion, i.e. the Gauss method for internal/external field separation, followed by Q-response estimation and inversion.

The regularization term introduced to tackle the model non-uniqueness and ill conditioning inherent of EM induction sounding problems has multiple interpretations. From a deterministic point of view, the Tiknonov matrix $\mathbf{\Gamma}$ in Eq. 2.9 and Eq. 2.43 alters the topography of the objective function, so that among the diverse models that yield predictions of data that are similar within a threshold (controlled by λ), the model with the least regularization term $\|\mathbf{\Gamma}\sigma\|_2^2$ is sought. From a probablistic point of view, it is equivalent to incorporating prior knowledge, in which case $\lambda\mathbf{\Gamma}^T\mathbf{\Gamma}$ is interpreted as the inverse of the (prior) model covariance $\mathbf{C}_\sigma^{-1}$. Here the 1st order finite difference operator is chosen, effectively maximizing model smoothness. The regularization strength λ controls the relative weight between the data misfit and the model roughness. Since it is a hyperparameter in inversion that cannot be determined *a priori*, a series of inversions are carried out with varying regularization strengths for each inversion scheme and the desired value of λ is chosen using the L-curve (Hansen and OLeary, 1993) to mitigate completely *ad hoc* choices.

Finally, we note that the absolute values of the data misfit for Q-response inversion and VP/alternating methods are not directly comparable. Even when the data misfit is normalized by the number of data samples, Q-response inversion and VP/alternating methods perform inversion with respect to different data. The latter approaches directly work on the observational data in the frequency domain, the uncertainties of which are propagated from the time-domain estimates, while the former is conducted on estimates of transfer functions and their formal uncertainties in regression. Therefore, the magnitudes of the objective function between Gauss and VP/alternating methods should not be directly compared. It naturally follows that the respective suitable regularization strengths are also not directly comparable in magnitude, and they are expected to vary between Q-response inversion and VP/alternating schemes. It is, however, worthy of noticing that VP and alternating methods, regardless of their variants, share the same data misfit evaluation, and are thus comparable in terms of data misfit as well as regularization strengths. Following the standard procedure, the choices of regularization

strengths are done separately for each scheme, but such choices may be general across different variants of VP and alternating approaches, as is indeed the case in the experiments shown later.

3.1. Synthetic experiment

Since both Q-response inversion and the VP/alternating approaches are done in the frequency domain, the same discrete frequencies are chosen for all inversions. In the case of synthetic test, 15 periods log-spaced between 1 and 100 days are chosen. The inducing field to be determined is parameterized as SH coefficients up to SH degree and order 3 at a subset of 30 observatories, and the electrical conductivity model is parameterized as a 15-layer 1D profile. Although the coherence of the Q-responses obtained by Gauss method is adequately high for all modes and frequency bands due to the ideal synthetic data (see e.g. Figs. B.3, B.4), only the degree-one response Q_1 is used for inversion afterwards. VP/alternating approaches, on the other hand, automatically try to fit all modes and frequencies simultaneously, as the observational magnetic field is viewed as the fitting objective in this schemes.

For VP methods, all three variants are tested in the process. For alternating approaches, four different linear update rules are tested: 1) the external field is estimated once at the beginning using some initial conductivity model, and never updated afterwards; 2) the external field is re-estimated every 10 iteration; 3) the external field is re-estimated every 5 iterations, and 4) the external field is updated following the Fibonacci sequence (that is, at iterations 1, 2, 3, 5, 8, ...). The alternating methods with these four linear update rules are hereinafter abbreviated as alt-∞, alt-10, alt-5 and alt-Fibonacci, respectively.

Most of the synthetic data inversions produce satisfactory results of the conductivity profile within ~ 20 iterations. In particular, we first look at two representative cases, namely full-VP and alt-Fibonacci, in addition to the reference Q-response inversion. These include the best-performing schemes within VP variants and alternating approach variants, as will be become clear in the results and discussions that follow. The recovered mantle conductivity profiles are shown in Fig. 3.1. The conductive lower mantle is recovered almost perfectly, especially in the case of full-VP and alt-Fibonacci, while the inverted upper mantle conductivity follows a gradual decrease from 600km depth upwards, and in these cases experience a mild reverse jump at lithospheric depths. As will be demonstrated later, the frequency bands of the data are most sensitive to the upper lower mantle, resulting in good constraints within the corresponding depth range, while the gradual depth-dependent upper mantle conductivity is largely due to the smoothing effect of the regularization applied. Q-response inversion generates a similar result,

with a mildly smoother upper mantle electrical conductivity and a slightly rougher lower mantle model. In general, the magnitudes of both the upper and the lower mantle can be recovered satisfactorily using VP and alternating approaches to the same extent as using Q-response inversion.

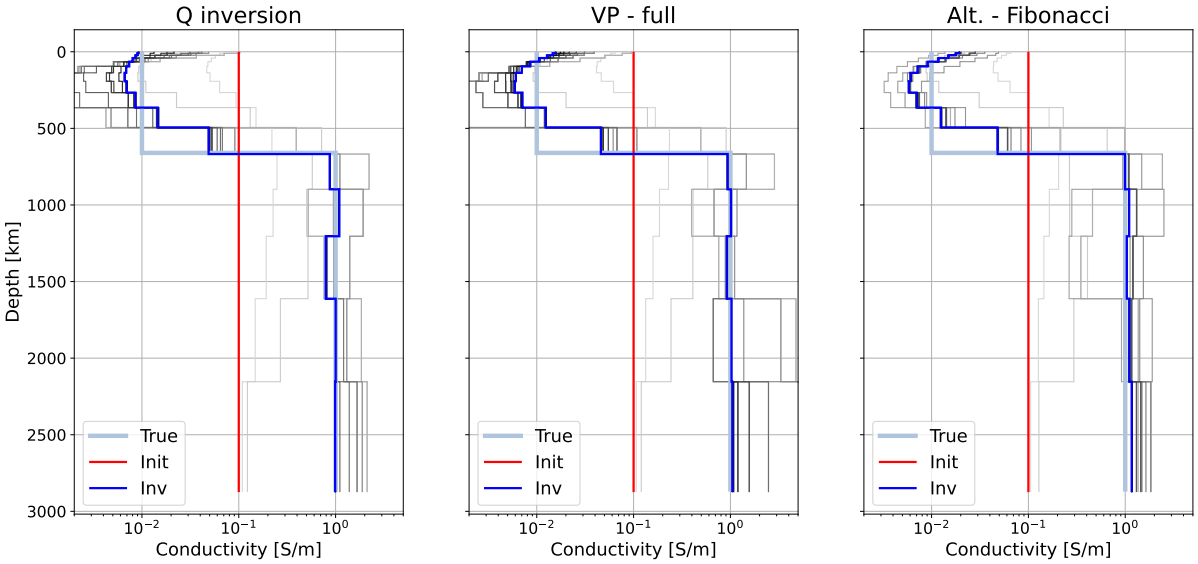

Figure 3.1.: Electrical conductivity profile recovered for representative inversion schemes. The results come from Q-response inversion (left), full-VP (middle) and alternating approach using the Fibonacci linear update rule (right). In each case the final inversion result (blue) is plotted together with the initial model (red) and the ground truth (light blue). The intermediate models along the iterations are also plotted in gray scale, color-coded by iteration numbers. Lighter lines correspond to earlier iterations, while darker lines correspond to later iterations.

One of the merits of variable projection inversions as well as alternating approaches is that they simultaneously produce the estimate of the linear model, i.e. the inducing field in this context, along with the mantle electrical conductivity. Since the inversions are carried out in the frequency domain, the linear model is estimated in the form of windowed spectrum $\varepsilon_n^m(\tau, \omega)$ (Eq. 2.35). In the synthetic test, the ground truth external coefficients are known, and hence can be used to validate the windowed spectrum of the inducing field SH coefficients inverted using these approaches. A comparison between the ground truth and the estimated external field using VP for modes $\varepsilon_2^1(\tau, \omega_i)$ and $\varepsilon_2^2(\tau, \omega_i)$ are presented in Fig. 3.2 and 3.3, respectively, with the three frequency bands presented being $\omega_i = 2\pi/T_i$ and T_i =1, 10 and 100 days. From visual inspection, our synthetic tests for VP yields an estimate almost identical to the ground truth, indicating almost perfect recovery of the windowed spectrum of the external field. This is

not limited to such frequency bands of spherical harmonic components with high field energies (e.g. the daily band $\sim$ 1 day for ε_2^1, Fig. 3.2 left panel), but applies to frequency bands with marginal energies (e.g. Fig. 3.2 right panel) or spherical harmonic coefficients with low energies (Fig. 3.3) as well. Similar results are observed for alternating scheme with Fibonacci linear update rule (Figs. B.1 - B.2).

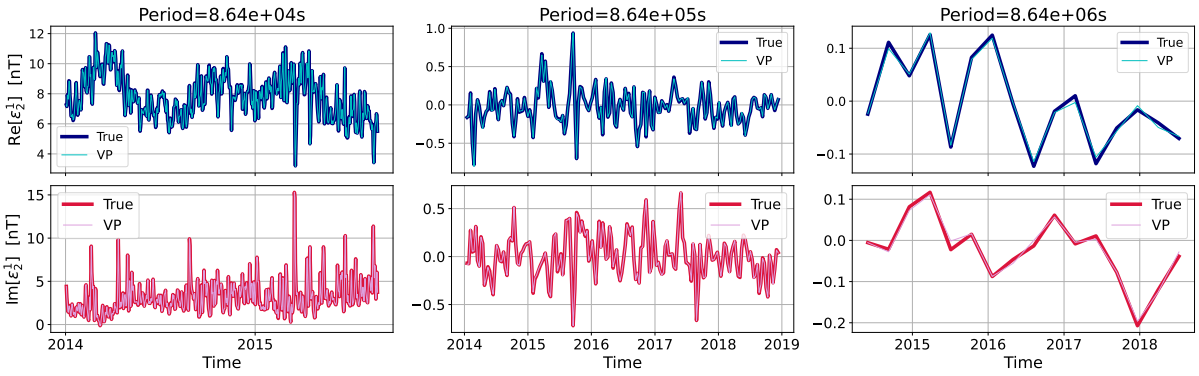

Figure 3.2.: Recovered inducing field coefficient ε_2^1 in the frequency domain using full-VP. Three frequency bands (left: 1 day; middle: 10 days; right: 100 days) are shown. The windowed spectra are split into real parts (upper panel) and imaginary parts (lower panel). In each subplot the inversion results (cyan for real parts and light pink for imaginary parts) are shown on top of the ground-truth windowed spectrum (thick blue and red lines).

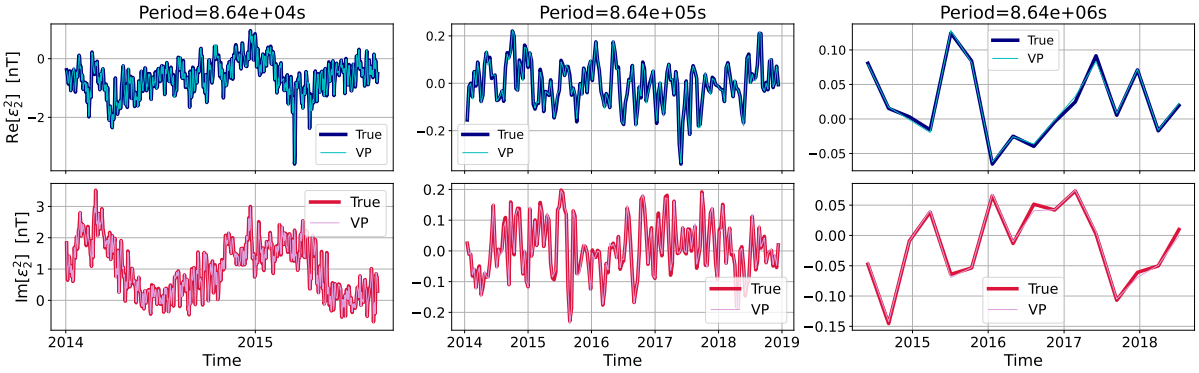

Figure 3.3.: Recovered inducing field coefficient ε_2^2 in the frequency domain using full-VP. The frequency bands and the legends are the same as Fig. 3.2.

It is hence demonstrated that with appropriate hyperparameters and specific variants, all types of inversion methods are able to yield satisfactory solutions on the synthetic dataset. Furthermore, the convergence behaviours are similar across these representative inversion schemes, as shown in the evolution of model roughness and root-mean-square (RMS) misfit (Fig. 3.4) and the period-wise evolution of RMS misfits (Fig. 3.5). All of these inversion cases (except for

alt-∞) converged to the stable solution within 20 iterations, not least due to the simple setup and perfect estimation of the error. Full-VP scheme and alt-Fibonacci scheme have reached a stationary solution at the 10th iteration, whereas Q-response inversion reaches one three iterations later. As a side note, full-VP is particularly fast in reducing the misfit, taking only 5 to 6 iterations to achieve a satisfactory solution in terms of RMS-misfit, although the regularization term still plays the role of reshaping and smoothing the solution in later iterations. In all cases, we observe an initial bulge of model roughness, followed by a gradual decrease, accompanied by an almost monotonic decrease of the data misfit. This behaviour is expected as the inversions start from a uniform model with zero roughness, thus they first attempt to fit the data at the cost of expanding model complexity, and then stabilize by settling for a smoother model after the data misfit reaches a certain level.

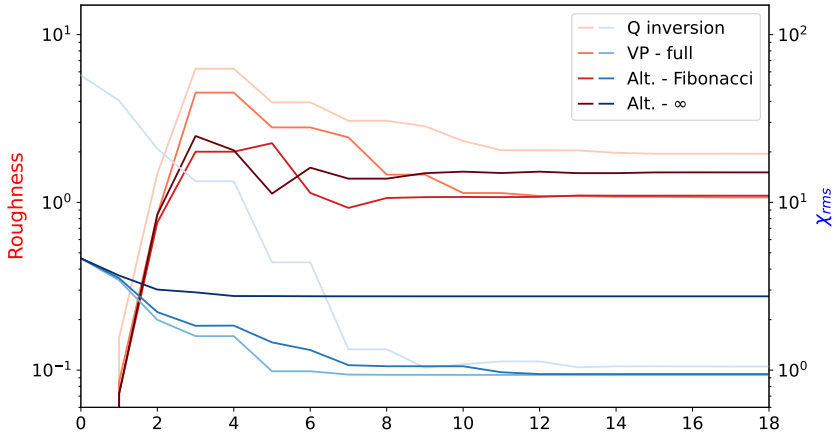

Figure 3.4.: Evolution of root-mean-square misfit and model roughness. The evolution of normalized RMS misfit (right axis) are plotted in blue, and the evolution of model roughness (left axis) plotted in red. Roughness is evaluated by calculating $\|\mathbf{\Gamma}\sigma\|_2^2$. From light to dark colors, the parameter evolution curves are plotted for Q-response inversion, full-VP, alt-Fibonacci scheme, and alt-∞ scheme, respectively.

In full-VP and alt-Fibonacci schemes, the converged models yield normalized RMS values (χ_{rms}) of 0.9361 and 0.9405, respectively (Fig. 3.4). This is a perfect indicator of successful data fitting, and at the same time justifies our method of estimating the uncertainty associated with windowed spectra (Eq. 2.47). As a side note, although the overall RMS misfits are close to one for both schemes as anticipated, this is not exactly the case for frequency-wise RMS misfits (Fig. 3.5), which range from 0.9 to 2.0 even for best-fitting models in this ideal synthetic scenario. Further investigation shows that even the ground truth model yields similar patterns of the RMS misfits for different frequency bands, suggesting systematic bias for the modelling process. This discrepancy is attributed to the inevitable spectral leakage in windowed Fourier domain

modelling (Appendix A). The discrepancy, however, does not seem to impact our final result notably, which is a sign that the overall error arising from this imperfect modelling process is much smaller than the synthetic error used to contaminate the dataset, not to mention additional modelling errors that are inevitably encountered in real datasets.

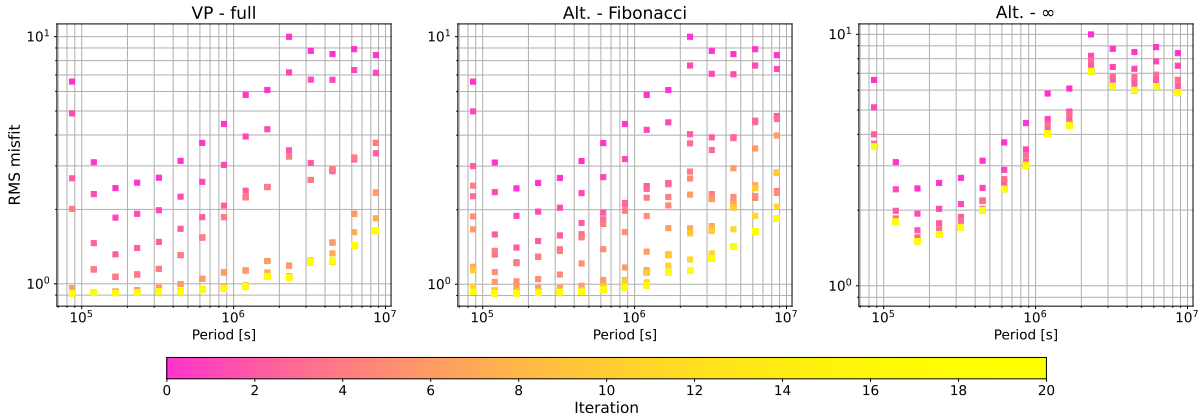

Figure 3.5.: Frequency-wise RMS misfits for full-VP (left), alt-Fibonacci (middle) and alt-∞ (right). In each plot, the RMS errors are color-coded by the iteration number.

As already stressed, VP and alternating approaches share the same objective function, in spite of the fact that the objective is formulated differently. Therefore, the manifolds formed by evaluating objective in VP and alternating approaches are all subsets of the manifold in the joint model space of σ and $\mathbf{c}$. The resemblance of the misfits and of the conductivity models (Fig. 3.1) obtained using these two methods hence reflects that both approaches succeeded in locating the same minimum in the joint model space. While in this simple example, both Q-response inversion and full-VP/alt-Fibonacci schemes converged to $\chi_{\mathrm{rms}} \approx 1$, the different approaches start from χ_{rms} values that are one magnitude apart (Fig. 3.4). This is again attributed to the distinct natures of Q-response inversion and VP/alternating approaches, which assign different meanings to the respective RMS misfits. As surrogate methods for joint model space inversion, VP/alternating approaches formulate misfits directly on the data; χ_{rms} hence indicates how much of the observational data is explained by the combination of the estimated electrical conductivity model and the inducing source. Due to the primary role of the inducing field, a considerable part of the data can already be accounted for by a reasonable estimate of the inducing field without resorting to refined conductivity model, leading to a relatively small χ_{rms} even at the initial model. TF inversion, on the other hand, directly fits the estimated TF, which is itself only related to the subsurface medium. The primary contributions from the inducing field to the observations have already been separated from the TFs, e.g. using Gauss method in this case. Therefore, χ_{rms} in this context only contains the second-order effect, and signals

how much of the TF is explained by the subsurface conductivity model alone, leading to a much larger RMS misfit at the initial model.

As our synthetic dataset comprises known inducing field models, we also examine how the inducing field estimates converge towards the ground truth solution for VP and alternating methods. We introduce the frequency-wise relative error for the SH coefficients, defined as

$$\epsilon_{\mathrm{SH}}^{nm}(\omega) = \sqrt{\frac{\sum_i \left|\varepsilon_n^{m,\mathrm{true}}(\tau_i,\omega) - \varepsilon_n^{m,\mathrm{est}}(\tau_i,\omega)\right|^2}{\sum_i \left|\varepsilon_n^{m,\mathrm{true}}(\tau_i,\omega)\right|^2}}. \tag{3.1}$$

The evolution of $\epsilon_{\mathrm{SH}}^{nm}(\omega)$ as a function of iterations for full-VP, alt-Fibonacci and alt-∞ are shown in Figure 3.6. While in VP the inducing field monotonically approaches the ground truth except for marginal oscillations around the converged solution, and eventually converges at iteration 6 for all presented modes using VP, slightly earlier than the conductivity model stabilizes, the inducing field does not converge until the 13th iteration using the alt-Fibonacci scheme. As a reminder, however, since alternating approaches do not update the inducing currents at each iteration, only 5 linear projections have been made by iteration 13 in alt-Fibonacci, following the Fibonacci linear update rule. Deterioration of the inducing field solution is also observed in the long periods when using the alt-Fibonacci scheme. For instance, the estimated inducing field has higher relative error at iteration 8 compared to iteration 5 for all presented modes at periods longer than 30 days (Fig. 3.6, middle column).

The alt-∞ shown here represents the worst inversion scheme. As this approach does not update the source estimate after the initial regression, the error of the inducing field remains the initial value throughout the process (Fig. 3.6), which in turn leads to stagnant RMS-misfit well above one (Fig. 3.4, 3.5). Although using such simplistic model as the initial model in our inversions may yield reasonable estimates of the field in some energetic modes where the primary contributions are sufficiently pronounced, the estimates become very problematic for long periods or weak modes (Fig. 3.6, middle and bottom rows), an issue which will be further examined in Chap. 4.

Previously we have focused on Q-response inversion and two representative schemes of VP and alternating approaches to compare model recovery and convergence behaviour. The difference between variants within VP or alternating approaches, on the other hand, is more pronounced, as we have alluded to in the comparison between alt-Fibonacci and alt-∞ schemes. Among variable projection schemes, full-VP is the scheme with the lowest degree of approximation

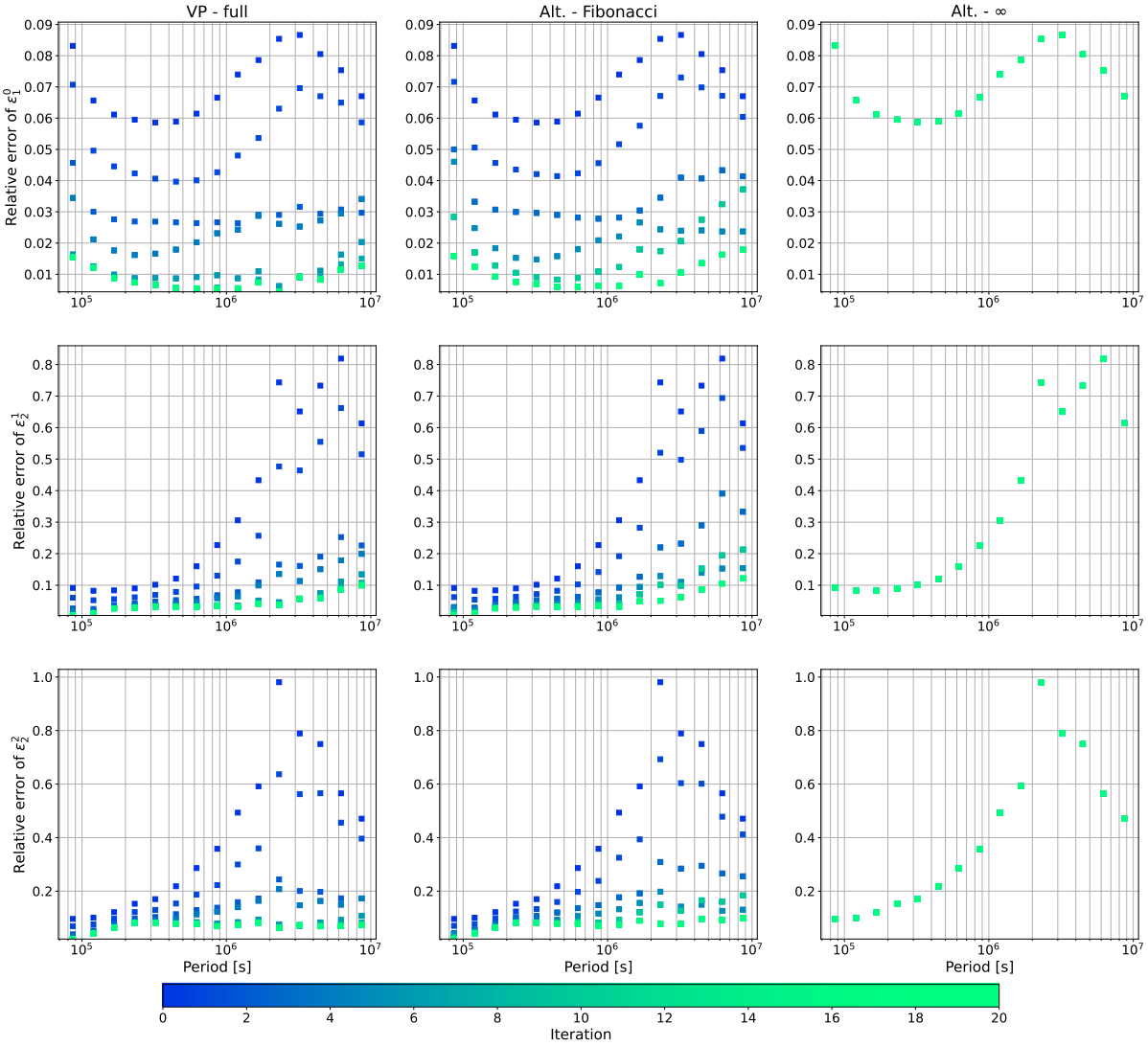

Figure 3.6.: Frequency-wise relative errors for different modes. The columns show the RMS errors using full-VP (left), alt-Fibonacci (middle) and alt-∞ (right), respectively. Different rows are for different modes, i.e. $(1, 0)$ (top), $(2, 1)$ (middle) and $(2, 2)$ bottom. In each plot, the relative errors are color-coded by the iteration number.

(the only approximation made is on the Hessian), and should in principle provide the best local constraint. This constraint is further simplified in VP-RW2, and is in the end completely abandoned in VP-RW3. Although different variants are observed to converge to almost the exact same electrical conductivity model that is satisfactorily close to the ground truth for the synthetic data (Fig. 3.7), it is indeed observed that VP-RW3 exhibits slower convergence for both linear (Fig. 3.8) and non-linear (Fig. 3.7) parts of the model. Most period bands of the external field take $8 \sim 10$ iterations to converge. Deterioration of the solution is also observed for VP-RW3 for periods longer than 10^6 seconds, similar to what is observed for alt-Fibonacci scheme, while such increase of the error is absent in full-VP and VP-RW2, consistent with the effect of increasing approximation levels. It is anticipated that poorer performance of VP-RW3 will be more pronounced for more complex and high-dimensional models.

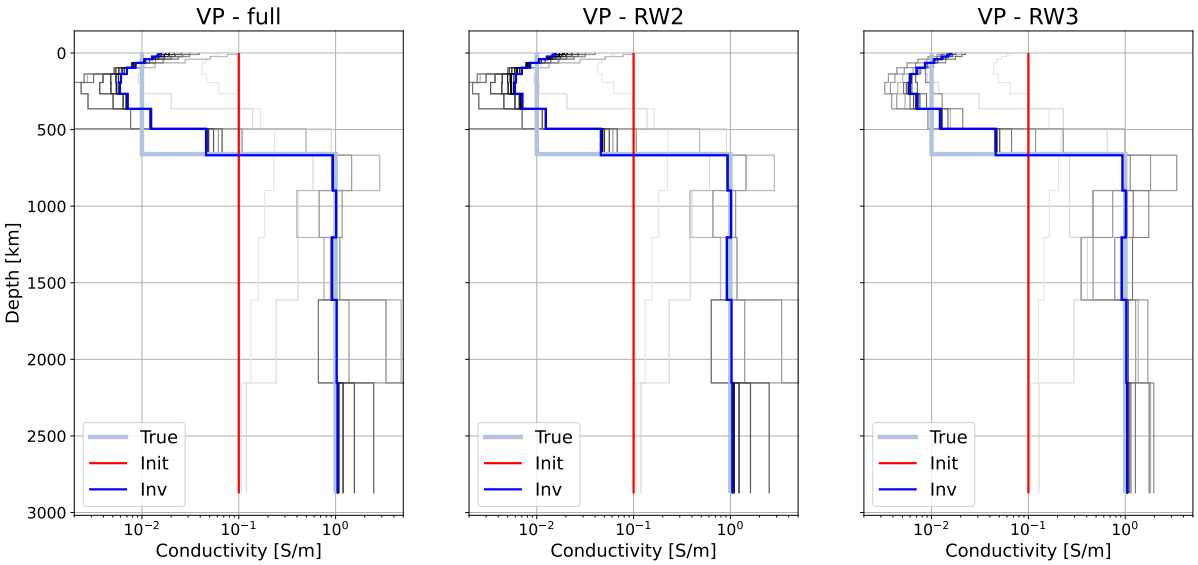

Figure 3.7.: Electrical conductivity profile recovery for variants of VP. The results come from full-VP method (left), VP-RW2 (middle) and VP-RW3 (right). The legends and the color coding of the intermediate models are the same as in Fig. 3.1.

Next, we look at the model recovery and convergence behavior of alternating approaches when the linear update frequency is decreased. As shown above, updating the inducing field coefficients at iterations in a Fibonacci sequence still allows the inversion to converge to a solution that is fairly close to the VP solution (Fig. 3.1) within 20 nonlinear iterations with only 6 linear updates, but as soon as the frequency is cut to every 5 iterations, considerable deterioration of the electrical conductivity recovery occurs, particularly in the lower mantle (Fig. 3.9). Not only is the inversion taking longer to reach a stationary point, but the scheme fails to locate the best fitting non-linear solution within 20 iterations as well, proving to be at best only half

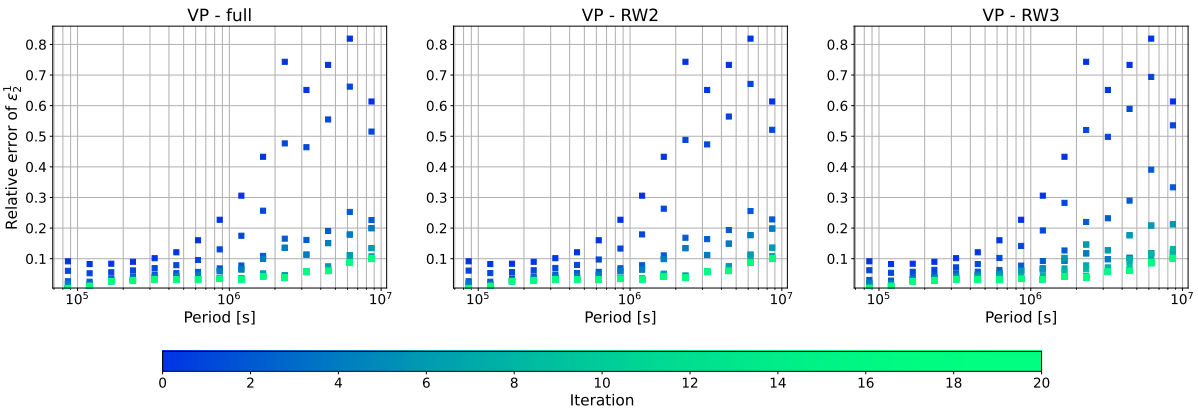

Figure 3.8.: $\epsilon^{21}_{\mathrm{SH}}(\omega)$ evolution for VP methods. The variants shown are full-VP (left), VP-RW2 (middle) and VP-RW3 (right).

as efficient as VP or alt-Fibonacci.

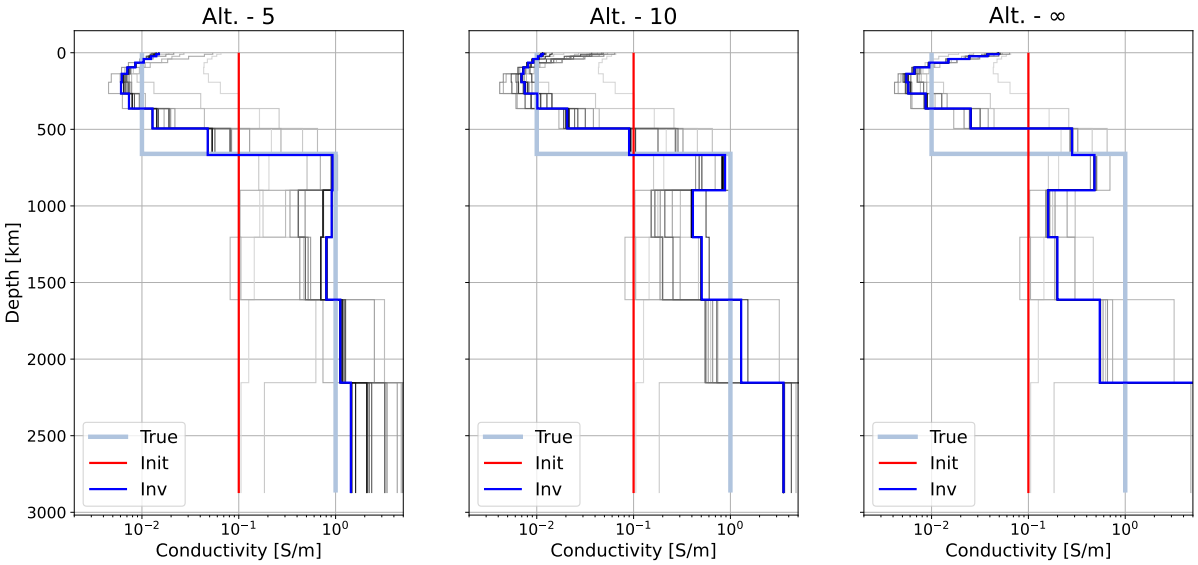

Figure 3.9.: Electrical conductivity models recovered using variants of alternating approaches. The variants either update the inducing source with a constant interval of 5 iterations (left, alt-5) or 10 iterations (middle, alt-10), or never update the source after initial estimation (right, alt-∞). The legends and the color coding of the intermediate models are the same as in Fig. 3.1.

Interestingly, despite the deteriorated recovery of the mantle conductivity, alt-5 produces an estimate of the external field that is comparable in accuracy to VP or alt-Fibonacci scheme (compare Fig. 3.10 with Fig. 3.6), with slightly increased errors only in some long period bands. However, as seen in Fig. 3.11, the misfit and the model roughness for alt-5 have already stagnated at the final stage, and the convergence criterion is satisfied at iteration 18,

indicating that the optimization has already converged. Therefore, the misfit between the ground truth and the inverted conductivity models (Fig. 3.9) is not due to non-convergence or failure in seeking the stationary point, but can only be attributed to the marginal difference in external field, and the final inverted conductivity profile should be considered the optimizer of the manifold constrained by the slightly incorrect external field. Alt-5 provides such a clear example where a relatively small error in the inducing source field leads to significant artifacts in conductivity model. When the number of linear updates are cut even further, both the external field estimation and the mantle conductivity recovery deteriorate further, as in the case of alt-10 and alt-∞ (Fig. 3.9 and 3.10).

It is worth mentioning that two types of convergence behaviors are observed in these experiments. In one common scenario, the model estimates along with the diagnostic parameters such as χ_{rms} and roughness either fulfill the convergence criterion, terminating the inversion, or oscillate mildly in the vicinity of a stationary value. The model is considered "converged" in this scenario, whether (as in VP-variants and alt-Fibonacci scheme) to the vicinity of the ground truth or to a local optimum (undoubtedly the case in alt-5) of the manifold in the joint model space. In another scenario (observed in the case of alt-∞), the objective is not improved for more than 10 iterations. This behavior indicates that the trust-region Newton method employed for optimization repeatedly rejected all update proposals, likely because of a poor local quadratic approximation and severe ill conditioning away from the optimum.

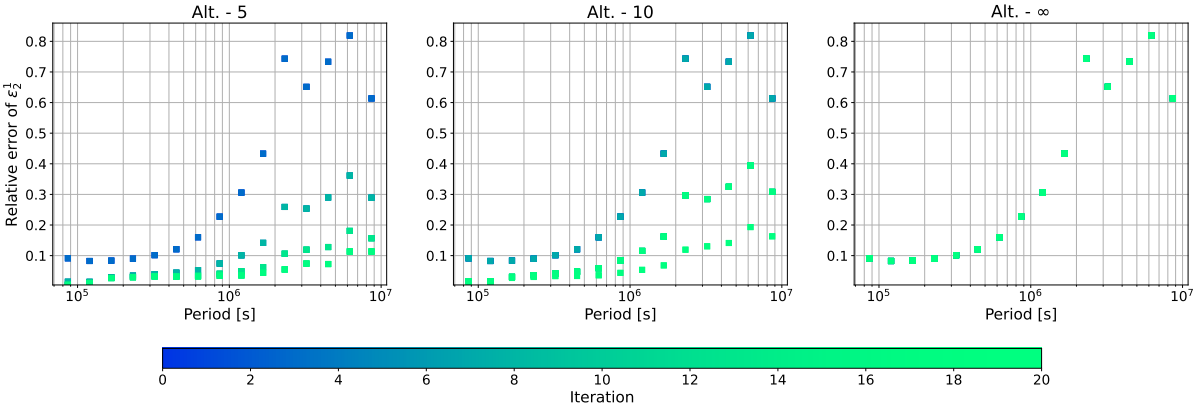

Figure 3.10.: $\epsilon_{\text{SH}}^{21}(\omega)$ evolution for alternating approaches. The variants shown are the same as in Fig. 3.9.

As a final perspective, we examine the dual property of Hessian matrices obtained using different methods. The Hessian matrix is the coefficient for quadratic approximation at a point for the objective function, and describes the local curvature of the function. Non-regularized Hessian is calculated directly using the Gauss-Newton approximation as $\mathbf{H} \approx \mathbf{J}^T\mathbf{J}$, with $\mathbf{J}$ being the

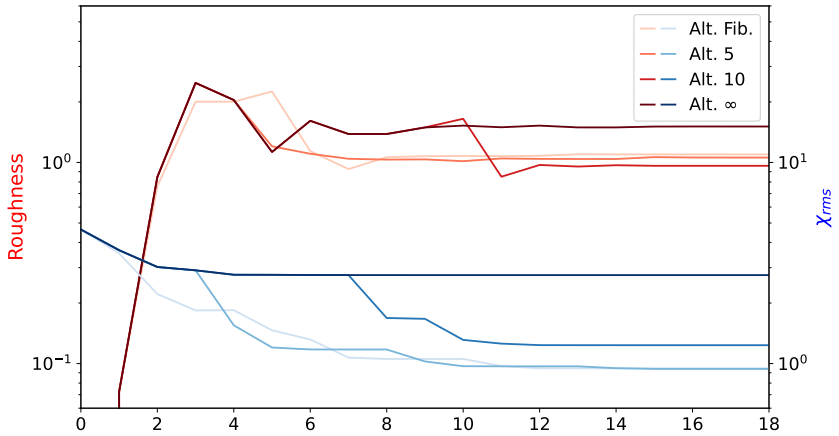

Figure 3.11.: Evolution of RMS misfit and model roughness. The displayed quantities and the calculation of roughness are the same as in Fig. 3.4. The curves are color-coded by inversion schemes, the lightest ones to the darkest ones corresponding to alt-Fibonacci, alt-5, alt-10 and alt-∞, respectively.

Jacobian matrix, constructed using Eq. 2.22, 2.24 or 2.25 in VP, or simply $\mathbf{H} \approx \mathbf{J}_\sigma^T \mathbf{J}_\sigma$ for alternating approaches. Hessian of the entire objective function, on the other hand, additionally contains the regularization term, and is given by $\mathbf{H}_{\text{reg}} = \mathbf{H} + \lambda \boldsymbol{\Gamma}^T \boldsymbol{\Gamma}$. The significance of Hessian is two-fold. First, it forms the linear system at each iteration in Newton methods, and controls the conditioning of the problem. The conditioning of the non-regularized Hessian is related to the topography of the misfit function and provides some measure for how ill-posed the problem constrained by the data is. VP and alternating methods are found to produce Hessian matrices that are slightly more well-conditioned compared to the Q-response inversion (Fig. 3.12), although the difference is marginal in the leading eigenvalues, and is only considerable for smaller eigenvalues. We do, however, observe that it is a consistent behaviour throughout the iterations, and is robust regardless of the data selection.

Secondly, in the framework of Bayesian inference, the regularization is considered as the inverse of the prior model covariance, and the Hessian can be reformulated as the inverse of the posterior model covariance

$$\mathbf{H}_{\text{reg}} = \mathbf{H} + \lambda \boldsymbol{\Gamma}^T \boldsymbol{\Gamma} = \mathbf{H} + \mathbf{C}_\sigma^{-1} = \widehat{\mathbf{C}}_\sigma^{-1}, \tag{3.2}$$

where $\mathbf{C}_\sigma = (\lambda \boldsymbol{\Gamma}^T \boldsymbol{\Gamma})^{-1}$ and $\widehat{\mathbf{C}}_\sigma$ are the prior and posterior model covariances, respectively. To facilitate a direct comparison between different approaches, the dimensionless resolution matrix can be introduced as a transfer matrix from the true model perturbation to the resolved model perturbation in the vicinity of a given model. The resolution matrix can be constructed from

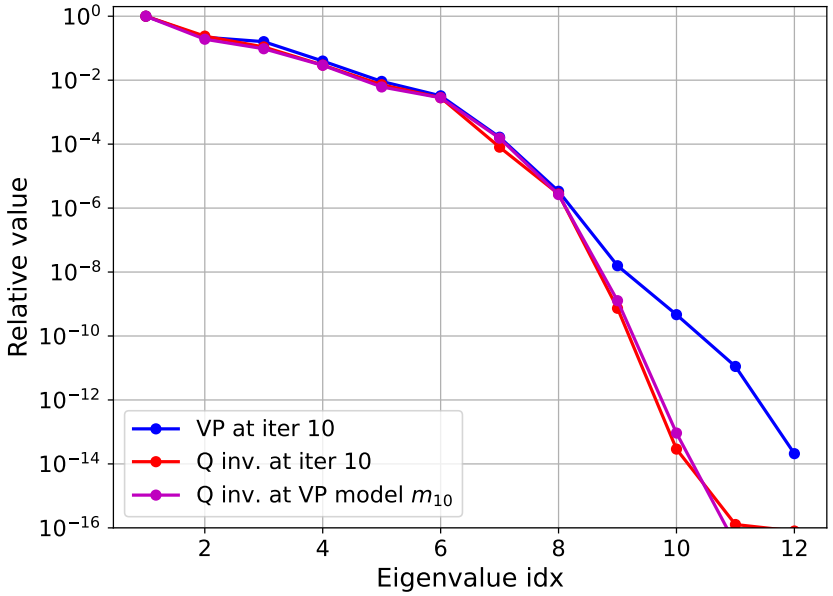

Figure 3.12.: Spectra of the Hessian matrices for Q inversion and VP method. The spectra are calculated by evaluating Hessian of Q forward modelling at the 10th iteration result of Q inversion (red), evaluating Hessian using VP at the 10th iteration result of VP inversion (blue), and evaluating Hessian of Q forward modelling at the 10th iteration result of VP inversion (purple).

the Hessian matrix as

$$\mathbf{R} = \mathbf{I} - \widehat{\mathbf{C}}_\sigma \mathbf{C}_\sigma^{-1} = \mathbf{I} - \mathbf{H}_{\text{reg}}^{-1} \left(\mathbf{H}_{\text{reg}} - \mathbf{H} \right). \tag{3.3}$$

Within the vicinity of the solution, the induced perturbation in the recovered model is related to the perturbation in the "true" model via the resolution matrix, i.e. $\delta\hat{\boldsymbol{\sigma}} = \mathbf{R}\delta\boldsymbol{\sigma}^*$, where $\hat{\boldsymbol{\sigma}}$ is the estimate of the model from inversion, $\boldsymbol{\sigma}^*$ is the true model, and δ denotes the perturbation in the respective models. A diagonal element of 1 indicates perfect resolution of the corresponding model parameter, and a value of 0 indicates virtually no resolution. Non-trivial off-diagonal elements contain the smearing effect between model parameters. We observe relatively high resolution (> 0.5) for 500 $\sim$ 2000km in the resolution matrices, with strong smearing of the electrical conductivity of the 1600 $\sim$ 2200km layer into the 2200 $\sim$ 2900km layer (Fig. 3.13), a feature ubiquitous in all inversion schemes. This general feature of the resolution matrix can be attributed to the bandwidth of the data. In our synthetic example, the frequencies cover two decades of periods from 1 day to 100 days, a band that is most sensitive to the depth of the MTZ (410-660km depth) and upper part of the lower mantle. Another demonstration comes from an alternative TF called the C-response, whose values and uncertainties can be trivially

converted from Q-responses via

$$C_n(\omega) = \frac{a}{n+1}\frac{1-\frac{n+1}{n}Q_n(\omega)}{1+Q_n(\omega)}$$
$$\delta C_n(\omega) = C_n(\omega)\frac{\left(1+\frac{n+1}{n}\right)\delta Q_n(\omega)}{\left(1-\frac{n+1}{n}Q_n(\omega)\right)\left(1+Q_n(\omega)\right)}. \tag{3.4}$$

With a dimension of length, the real part of the C-response corresponds to the central depth of induced currents, and is hence indicative of the penetration depth of the EM field at a certain frequency. The Q-responses estimated via SHA and the corresponding C-responses are shown in Fig. 3.14, indicating penetration depths ranging from 600km at diurnal band to 1500km at 100 days. As seen from previous examples, the electrical conductivity within this depth range is best constrained (Figs. 3.1 and 3.7). This is true even in the alt-5 inversion scheme (Fig. 3.9) where the model recovery is overall not ideal. Apart from that, slight improvements can be identified in VP/alternating resolution matrices compared to the Q-response inversion. Whereas only depth range 700 $\sim$ 1200km have resolution higher than 0.7 in the Q-response inversion result, both VP and alternating approaches extend such high resolution up to 1600km. At the same time, VP/alternating schemes also suppress smearing between electrical conductivities of adjacent layers compared to Q-response inversion, leading to two diagonally dominant elements in the resolution matrix.

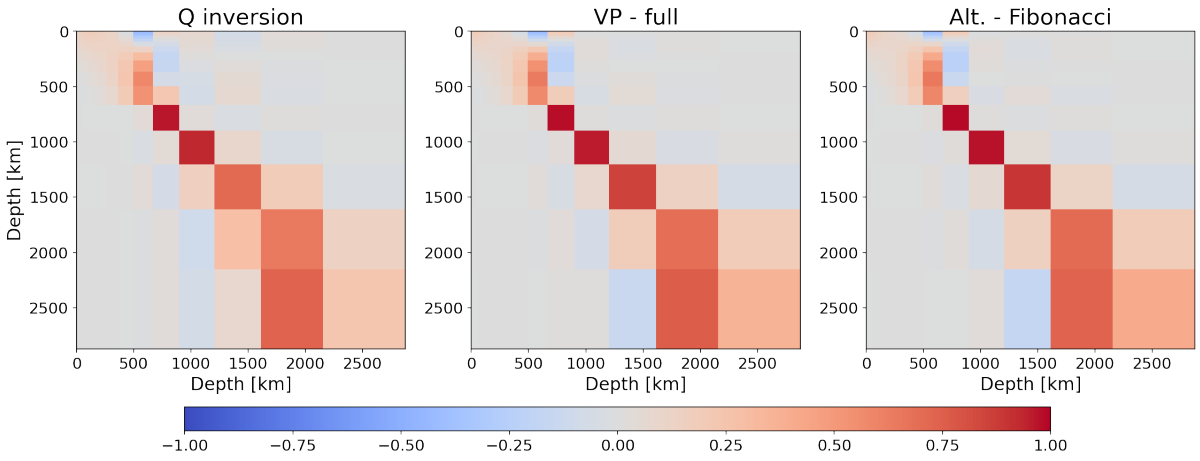

Figure 3.13.: Resolution matrices for representative inversion schemes. The resolution matrices are calculated for the best-fit 1-D mantle conductivity models consisting of 16 layers as obtained by applying the Q-response inversion and Gauss method (left), full-VP scheme (middle) and alt-Fibonacci (right), respectively.

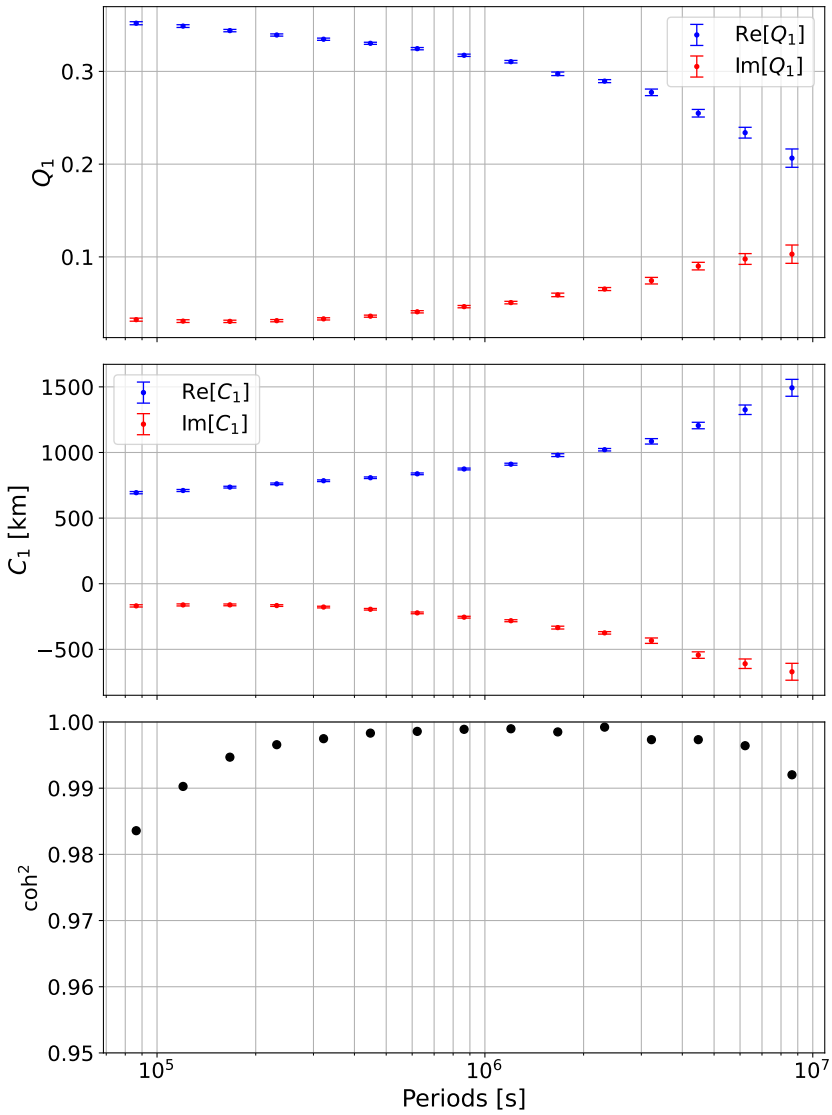

Figure 3.14.: Q-responses (top) and C-responses (middle) of degree 1 estimated from SH coefficients of mode $(1, 0)$. The error bars indicate the uncertainties associated with the estimates. The squared coherence of the transfer functions are shown in the bottom panel.

3.2. Real data inversion

The variable projection method is applied to the real ground geomagnetic observatory data collected between years 2014-2018 in order to simultaneously reconstruct mantle conductivity and external field spectrum. Several amendments are introduced to the pipeline used in numerical experiments so as to tailor the method to real-Earth probing purposes. First, a new semi-diurnal band (12 hours) is added to the aforementioned 15 frequency bands spanning two decades. This is used for improving constraints to the asthenospheric conductivity. Second, the parameterization of the mantle conductivity is expanded to a 45-layer 1-D profile. Following the practice of Grayver et al (2017), a fixed surface layer with the conductance of 6600 S is introduced, representing an average ocean-sediments conductance over the globe.

The data comes from 120 geomagnetic observatories within the mid-low geomagnetic latitude range of $5^\circ \sim 56^\circ$. During preparation of the windowed spectrum of the field observations, the observatory data in each time window are thresholded with 99% valid data and the missing observations are linearly interpolated before the windowed spectral transform (Eq. 2.40). For real time series of the magnetic field from observatories, no information on either the spectral or temporal properties or the magnitude of the noise is known. It is apparent that when a Gaussian white noise is assumed, the noise magnitude serves as a mere normalizing factor for the data misfit (Eq. 2.47), but would not alter the geometry of the objective function. It then follows that the behaviours in inversions (convergence, results, etc.) are invariant with respect to the assumed noise level, except for a corresponding scaler for the regularization term. Meanwhile, the spectral and temporal behavior of the unknown noise poses a much greater threat. Without the Gaussian white noise assumption, the estimation of the Fourier-domain uncertainty (Eq. 2.47) would be invalidated. Nevertheless, for practical purposes, a Gaussian white noise is still assumed for the real observations, and a standard deviation of 1nT is hypothesized.

The Q-responses and the corresponding C-responses of degree one are shown in Fig. 3.15. In sharp contrast to the synthetic experiment where the coherence is sufficiently high for virtually all modes and frequency bands, the real dataset yields considerably lower coherence for certain frequency bands. This is closely related to the dominant modes of the source. For instance, the diurnal band (24 hours) is dominated by ionospheric signals, which has a strong $(2, 1)$ SH component. Estimates of Q-responses using other modes, including the first zonal harmonic, will be strongly contaminated and biased due to relatively low energies, as shown by the low coherence and spurious jump in the TF values of Q_1 in the diurnal band (Fig. 3.15). It is therefore not sensible to use all frequency bands of Q_1 for Q-response inversion. Instead, via

thresholding the coherences, the following period bands are chosen: the period bands starting from 33 hours to 100 days of Q_1 estimated from SH mode $(1, 0)$, the period bands of 24 and 33 hours of Q_2 estimated from SH mode $(2, 1)$, and the period band of 12 hours of Q_3 estimated from SH mode $(3, 2)$. These combinations of period bands and SH modes have high coherence (see also Figs. B.5 and B.6), and are considered reliable for inversion.

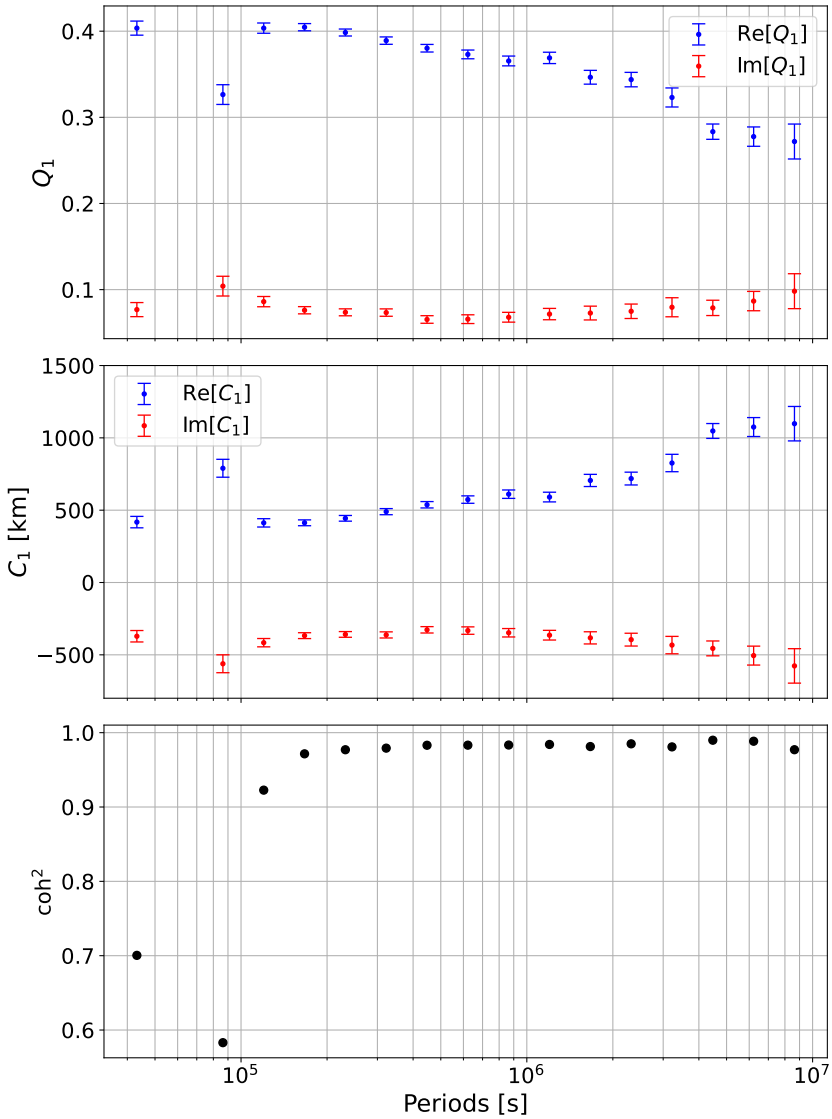

Figure 3.15.: Q-responses (top) and C-responses (middle) of degree 1 estimated from SH coefficients of mode $(1, 0)$ in the real dataset. The error bars indicate the uncertainties associated with the estimates. The squared coherence of the transfer functions are shown in the bottom panel.

A series of inversions are conducted with varying regularization strengths (Fig. 3.16, Fig. 3.17). For full-VP, all inversions eventually converged around 20 iterations, but some converged to sub-optimal solutions, probably local optima (regularization strengths 1.0×10^{-3} and 1.7×10^{-3}).

The local optimum issue is even more pronounced in the case of Q-response inversion (Fig. 3.17), where one can assert both the inversions at $\lambda = 32$ and $\lambda = 100$ converged to local minima, whose RMS-misfit is considerably larger than the solution obtained using $\lambda = 320$. Also obvious is the fact that unlike the synthetic tests, the VP inversions on the real dataset converged at models with RMS-misfits $\chi_{\text{rms}} \approx 11.7 \gg 1$. We however notice that the absolute reduction of RMS-misfit ($\Delta\chi_{\text{rms}} \approx -2$) is comparable to that of synthetic tests. In the end, the regularization strengths of 0.32 and 320 are chosen for the preferred VP model and the Q-response inversion model, respectively. These regularization strengths yield results located at the kinks of the respective L-curves, and are considered to give reasonable trade-off between data misfit and model complexity.

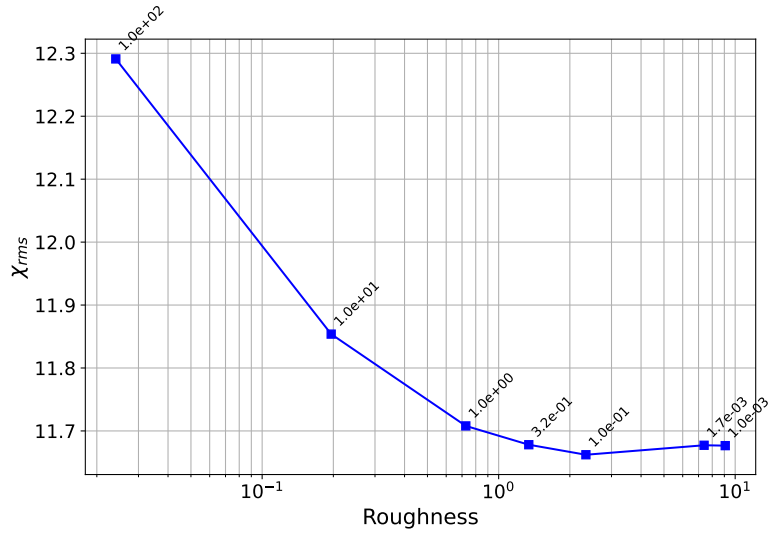

Figure 3.16.: L-curve of model roughness $\|\boldsymbol{\Gamma\sigma}\|_2^2$ and RMS-misfit for full-VP.

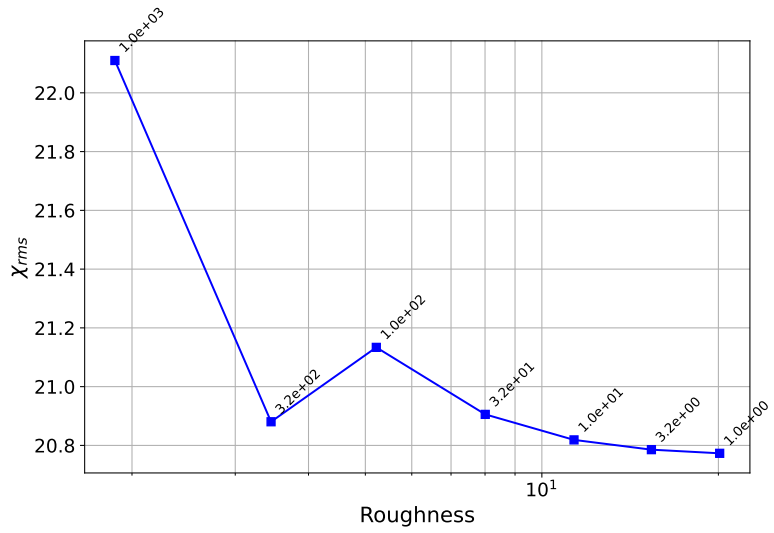

Figure 3.17.: L-curve of model roughness and RMS-misfit for Q-response inversion.

The VP inversion result (Fig. 3.18 right panel) shows a resistive upper mantle where the electrical conductivity monotonically increases from down to $10^{-4} \sim 10^{-3}$S/m near the surface of the Earth to 1S/m at the bottom of the MTZ. The maximum mantle conductivity at 750km depth just beneath the MTZ reaches $2 \sim 3$S/m, characterized by a conductive peak, a feature that is ubiquitous when using weaker regularizations. Beneath this conductive layer, the lower mantle is characterized by a resistive kink, followed by a mildly increasing conductivity profile, from $\sim$ 1S/m at 1200km depth to 2S/m at 2000 to 2500km depth.

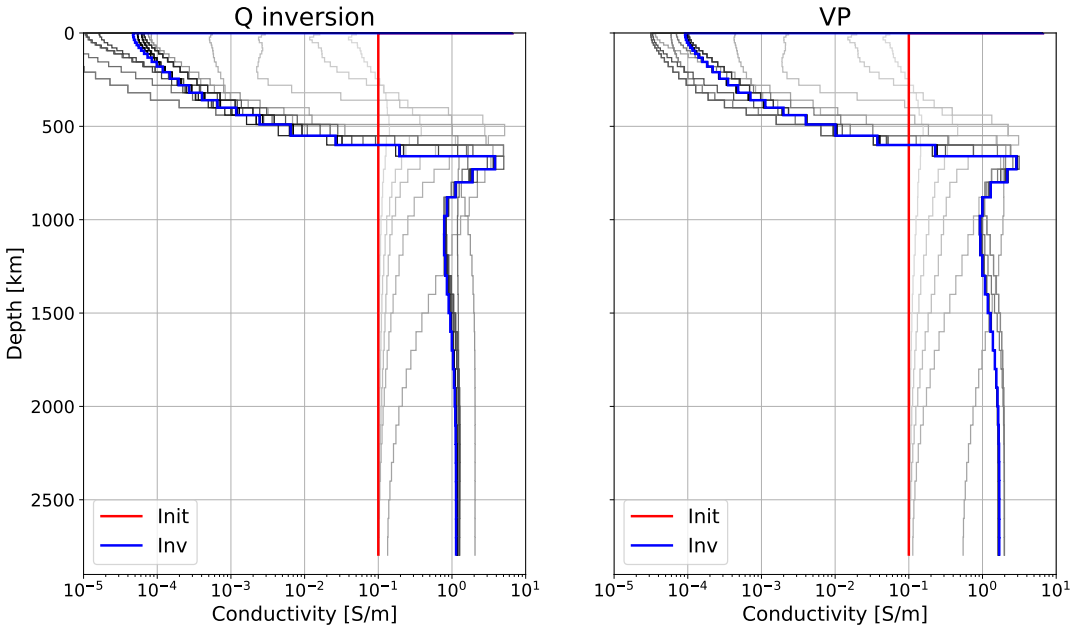

Figure 3.18.: Mantle conductivity obtained from ground observations within time period 2014-2018, using Q-response inversion (left) and variable projection inversion (right). The legends and the color-coding of the intermediate inversion steps are the same as in Fig. 3.7. A surface layer with electrical conductance of 6600S is kept fixed throughout the inversion.

The general pattern of the 1D profile obtained using VP agrees well with that obtained in the Q-response inversion (Fig. 3.18 left panel), especially in the MTZ and the upper lower mantle, a depth range to which the high sensitivity of the data is confirmed by the C-response (Fig. 3.15) and the respective resolution matrices (Fig. 3.19). The C-response of degree one shows that the penetration depth of the EM field ranges from 500km to 1200km in these frequency bands. A similar pattern is observed in the resolution matrix, with highest resolution at 750km depth, and limited resolution extending to 1300km. In the upper mantle or the deeper lower mantle, however, our data shows weak resolution. In the lower-right block of the resolution matrices, a curved band of positive elements fill the lower triangular part, indicating strong

smearing effects, owing to both the frequency band of the data and the regularization applied. As a result, the recovered electrical conductivity model in the deeper lower mantle is strongly affected by the overlying layers. We therefore conclude that the features recovered within the depth range of 500 to 1300km is robust; these include the significant conductivity increase with depth in the MTZ, the conductive layer in the uppermost lower mantle, which are consistent features between the Q-response inversion and the VP inversion. The electrical conductivity in the upper mantle as well as in the lowermost mantle are however not well constrained by the data.

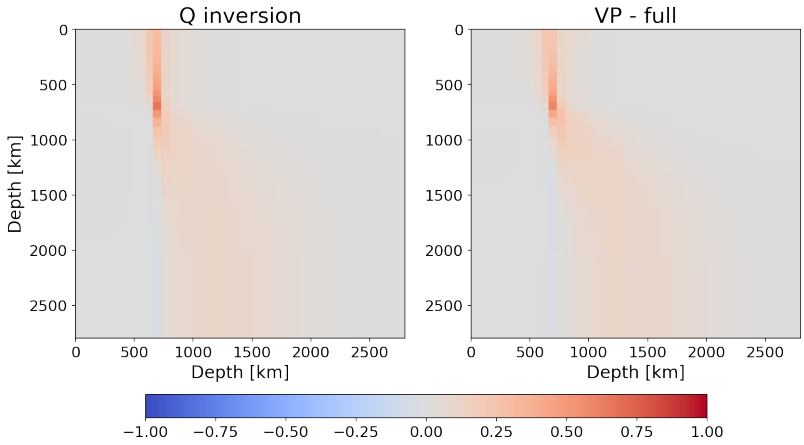

Figure 3.19.: Resolution matrices for the real data, using Q inversion and VP scheme. The resolution matrices are calculated for 44 layered mantle conductivity model at the respective inverted models.

As in the synthetic tests, the windowed spectra of the external field SH coefficients up to degree and order 3 are acquired in the VP inversion. The field estimation is roughly consistent with that obtained by field separation in Gauss method (Fig. 3.20), but its consistency is highly dependent upon the energy of the mode. For energetic spatial modes, e.g. periods longer than one day of ε_1^0 and diurnal bands of ε_2^1, etc. the results are highly consistent. Modes with low powers, e.g. 100 day period band for ε_2^1, show large discrepancies, although the recovered trends are still correlated. The consistency of different modes and frequencies seems to be correlated with the coherence distribution in Q -response estimation. Similar to the relative error defined in Eq. 3.1, a relative measure of the discrepancy of the estimated SHc coefficients can be introduced as

$$\epsilon^{nm}_{\mathrm{VP-Gauss}}(\omega) = \sqrt{\frac{\sum_i \left|\varepsilon_n^{m,\mathrm{VP}}(\tau_i,\omega) - \varepsilon_n^{m,\mathrm{Gauss}}(\tau_i,\omega)\right|^2}{\sum_i \left|\varepsilon_n^{m,\mathrm{Gauss}}(\tau_i,\omega)\right|^2}}, \tag{3.5}$$

where the superscripts indicate the methods with which the external SH coefficients are esti-

mated. The frequency-wise relative difference for mode ε_2^1 is shown in Fig. 3.21. The frequency bands of ε_2^1 with the least relative difference between the Gauss method estimate and our VP estimate are exactly the two bands whose coherences are higher than 0.9 in the Q-response estimation (Fig. B.5) and are subsequently included in the Q-response inversion. Similar correlations are observed in other modes as well (Figs. B.7, B.8). Therefore we conclude that for SH modes and frequency bands with high coherence of Q-response, the VP method should yield inducing source estimates that are consistent with that obtained using SHA in Gauss method.

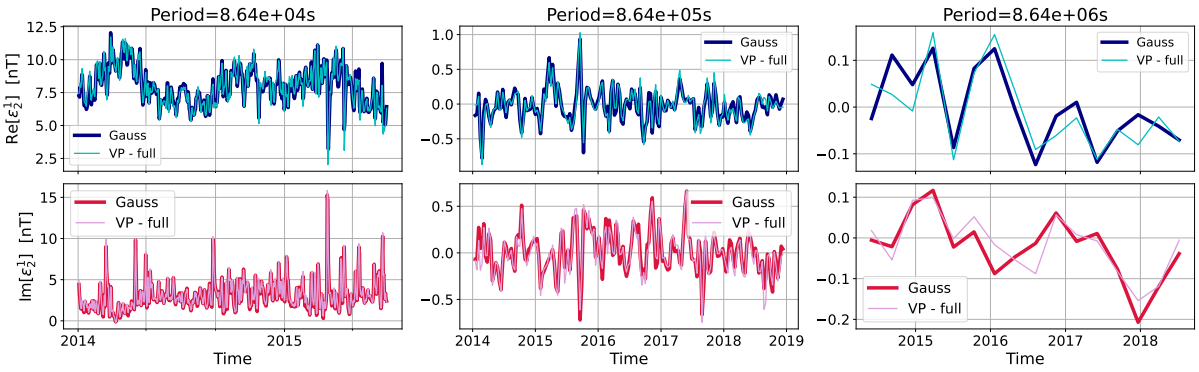

Figure 3.20.: Recovered inducing field coefficient ε_2^1 in frequency domain. The frequency bands are the same as Fig. 3.2. Each subplot shows the VP inversion results (cyan and pink lines) on top of the windowed spectra of the external field obtained by Gauss method (thick blue and red lines).

The correlation between the TF coherence and the inducing source consistency does not come as a surprise, but is a natural consequence of the physical connection between the inducing field and its induced counterpart. While VP explicitly demands that the forward modelling governed by the Maxwell's equation be used to directly explain the magnetic field observations, SHA in the Gauss method does not require such causal link between the estimated internal and external fields. It is only in the stage of TF estimation that such physical connection is established, and coherence is used to describe how much of the internal field can be causally explained by the forward operator, which in our case is the Q-response. Therefore, in frequency bands and SH modes where such physical connection is appropriate for explaining the data (i.e., high coherence), the inducing source estimate in the Gauss method should be close to that obtained in VP (i.e. low difference).

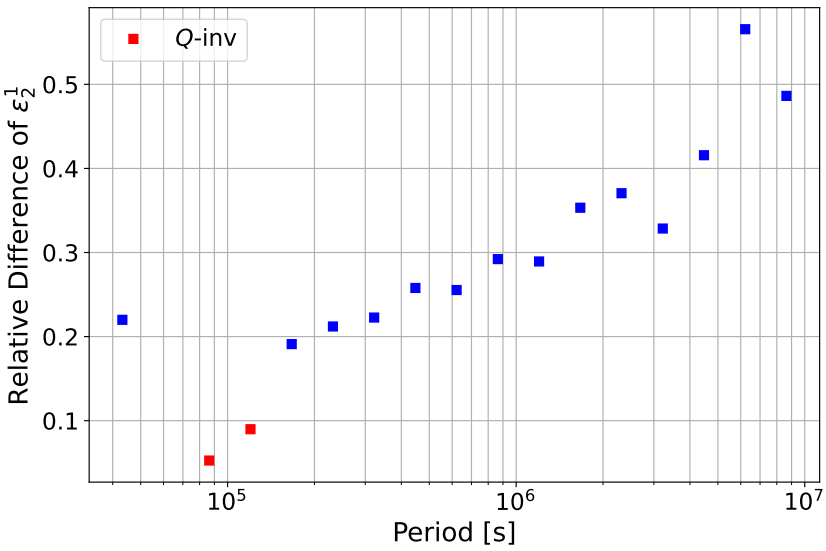

Figure 3.21.: Relative differences of inducing field coefficient ε_2^1 between Gauss method and VP inversion. The red squares mark the frequency bands in this SH mode which have a coherence over 0.9 in Q-response estimation, and are thus included in the Q-response inversion.

4. Discussion

It has been shown in the numerical experiments that the implementations of VP and alternating approaches are capable of producing inversion results that are at least equally good as, and in several aspects better than, the recovered mantle conductivity obtained in Gauss method and Q-response inversion with the same forward model in essence, while at the same time propagates the uncertainty of the data to the recovered models in a consistent manner. Both VP and alternating approaches provide an estimate of the mantle conductivity model and an estimate of the external field at each iteration, and provide insights as to the interplay between two model spaces.

4.1. Effect of linear update and derivative approximation

Both VP and alternating approaches provide efficient means to find a suitable solution in the joint model space by introducing point-dependent constraints. Whereas variable projection variants re-estimate the local "optimal" constraint at each iteration, alternating approaches allow a user to delay the next re-projection of the linear model and re-estimation of the constraint, implicitly assuming that the constraint remains valid at each subsequent iteration that reuses the initial projection. Although this saves resources and time, it is observed that such assumption may not be valid and can potentially cause considerable deterioration of the solution. Excessive nonlinear iterations using a fixed external field model may lead a conductivity model to deviate from an optimal solution, which in turn projects the inaccuracy back to the external field at the next iteration (Fig. 3.6, Alt. - Fibonacci). In real settings, without information about the ground truth, detecting such behaviour is practically impossible. Therefore, appealing though the alternating approach might be due to its simple nature, insufficiently frequent updates of the linear model (and with it the constraint) creates a risk of failed convergence, as was demonstrated in this study. On the other hand, more elaborate update rules, such as alt-Fibonacci, succeed in locating the optimal solution. This process is facilitated by more frequent linear updates at the early stage of the inversion. Therefore, alternating approaches should be used with care; in particular, for a given source model, the non-linear inversion on the conductivity model should not be run until it stagnates, by which time the conductivity model (and with it, the estimate of the external field) is probably already biased. In contrast, it is beneficial to alternate between conductivity inversion and inducing field estimation as often as possible initially, and only allow the linear model to freeze for more iterations at later stages.

In addition, the variants with different approximations of the Jacobian are tested in the VP framework. For our rather simple synthetic tests, no significant difference is observed between the models obtained with different VP variants. However, a slower convergence for the VP-RW3 variant is indeed observed (Fig. 3.8). Different levels of approximation of the Fréchet derivatives seem to work equally well for the synthetic experiment, and in practice it might be beneficial to adopt either VP-RW2 or VP-RW3 variants for the sake of computational efficiency, especially when evaluation of $\mathbf{DF}$ is expensive (to be the case once full 3-D forward operator is required, e.g. if we drop 1-D conductivity parameterization).

4.2. Interplay between conductivity model and external field

The external field model and the mantle conductivity model are mutually dependent in the optimization problem defined in Eq. 2.9. In particular, the mantle conductivity model is sensitive to perturbations in the external field, as was evident in the experiments where alternations between linear and non-linear models are done at varied frequencies (alt-Fibonacci, alt-5, alt-10 and alt-∞). Note that the application of the VP method completely eliminates this problem, and preserves consistency between the linear and non-linear model unknowns. It does not mean that the VP is less ambiguous than the alternating approach, but it allows one to attain the best (in the least-squares sense) possible trade-off between source and conductivity models.

In turn, mantle conductivity has a non-negligible feedback on source reconstruction. Naturally, currents induced in the conducting subsurface represent a second-order effect in observable fields (there are exceptions to this observations, related to the presence of strong lateral conductivity contrasts). Therefore, estimation of the source can produce reasonable results even for very simple conductivity models, at least in regions far away from 3-D conductivity variations, such as a uniform mantle conductivity of 0.1S/m, which is used as the starting model of all our inversions, or a simplistic two-layer Earth model consisting of a 1200km thick perfectly insulating mantle and a perfectly conducting core, hereinafter referred to as the bilayer model. For the perfect insulator-conductor bilayer model, the Q-response of degree n is a constant given by

$$Q_n = \frac{n}{n+1}\left(1 - \frac{h}{a}\right)^{2n+1}, \tag{4.1}$$

where h is the thickness of the overlying perfectly insulating layer. Due to its simplicity, the bilayer model is often used in space physics to provide first-order approximations of the induction effects. Indeed, such attempts are not completely unjustified, as despite their drastic difference from the synthetic ground truth, both conductivity models prove to yield reasonable estimates

of the external field windowed spectra that are roughly coherent with the ground truth external field spectrum (Fig. 4.1), even for frequency bands in higher degree modes with limited energies.

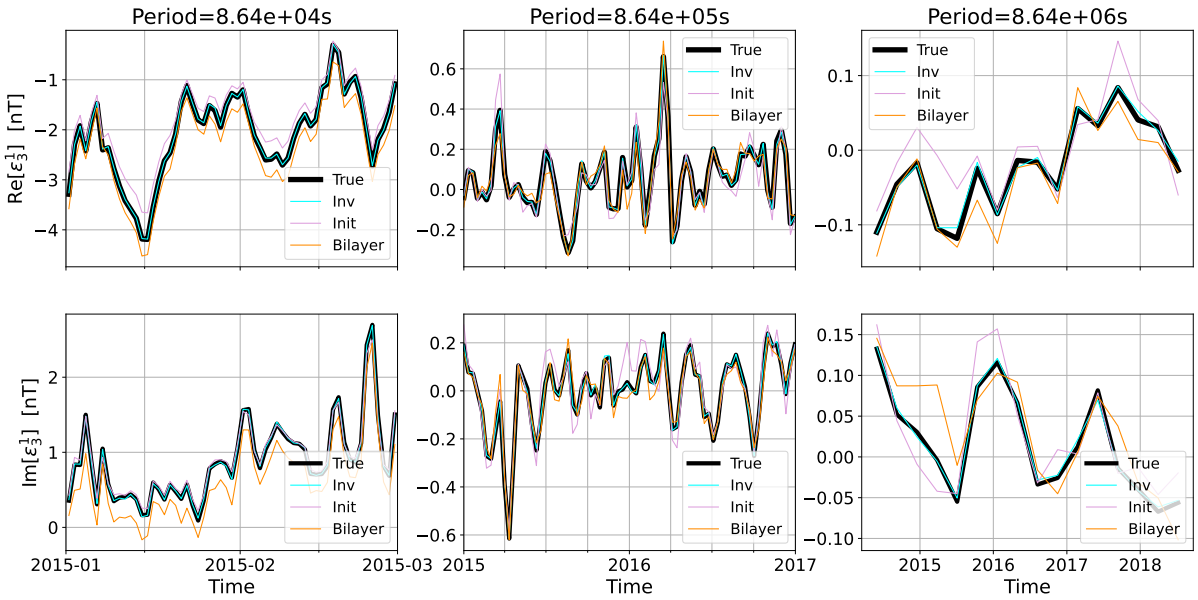

Figure 4.1.: Estimated windowed spectrum of the inducing field coefficient ε_3^1. Frequency bands are the same as in Fig. 3.2. For each frequency band, the inducing field coefficients are shown for the VP inversion result (cyan), estimation using a uniform mantle conductivity of 0.1S/m (magenta) and a simplistic perfect insulator-conductor bilayer model (orange). The estimations are produced using the synthetic data, and are plotted on top of the the ground truth (black).

That being said, there are considerable and noticeable discrepancies between the inducing field estimates using simplistic models and the ground truth field, for instance the amplitude discrepancies of the field recovered using the two-layered conductivity, especially in short (e.g. 1 day) and long periods (e.g. 100 days). The discrepancies are also obvious from the relative field errors evaluated in energies (Fig. 4.2), calculated from Eq. 3.1. While the inversion result from VP gives an external field ε_3^1 that is on average 5% different from the ground truth in most frequency bands, the aforementioned simplistic models yield external fields that are typically over 15% different from the true external field. The initial uniform conductivity model, for instance, gives relative inducing field errors of 15% in short periods, which increases to dramatic errors of 90% in periods around one month. For the simplistic two-layer model, the relative error of the external field increases from 20% in the diurnal band, to 45% in the period bands of one to three months. This large discrepancy is partially attributed to the low energies in these frequency bands of ε_3^1, but the different is considerable even for more energetic modes where all external field estimates are overall better constraint (see Figs. B.9 and B.10). In short, although the

sensitivity of the inducing field with respect to conductivity perturbations is not as pronounced as the other way around, those field estimates calculated using overly simplistic conductivity models are prone to additional relative error of magnitude $\sim$ 10% to 80%, which might vary depending on the quality of the approximation for the medium response in the frequency bands and modes of interest.

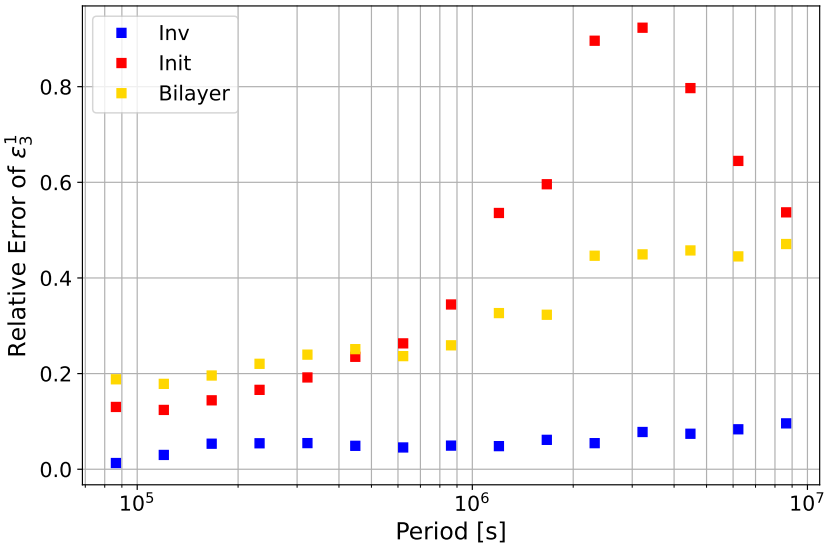

Figure 4.2.: Relative errors of the external field coefficients ε_3^1 with different conductivity models. Errors are shown for the VP inversion result (blue), estimation using a uniform mantle conductivity of 0.1S/m (red) and a simplistic perfect insulator-insulator bilayer model (orange).

4.3. Outlook

The numerical experiments and inversions in this thesis are confined to observations of ground observatories and a conservative model parameterization. The VP and alternating methods, however, are generalizable in both the observational and the parameterization aspects. The forward modelling in this study uses a 1-D parameterization of the Earth's mantle, which allows use of spherical-harmonic-order-independent Q-response and efficient frequency-domain modelling. In addition, the external field estimates are confined to large-scale spatial modes, up to order 3. While such models are adequate for demonstrational purpose and prove very tractable in numerical experiments, the real observations made on top of a heterogeneous Earth certainly contain non-negligible 3-D effects and contributions from more fine-scaled spatial modes of the external current system. This is clearly shown in the irreducible misfit with $\chi_{\text{rms}} \gg 1$ for the real data inversion (Fig. 3.16). The modelling error can be improved by including higher degrees of

time harmonics as well as using realistic 3-D models. Both generalizations would significantly increase the computational expense as well as dimensionality of the model space, which motivates the use of simplified VP schemes (VP-RW2/VP-RW3) or alternating approaches. While it is shown in the numerical experiments that different variants of VP schemes and sophisticated design of alternating approaches yield similar results and converge to the same optimum, the behavior of these variants on a higher dimensional conductivity model is yet to be confirmed.

Since neither VP nor alternating approaches, in their essential forms, make any explicit assumptions on the internality or externality of the fields, they have the capacity of incorporating both ground observatory data and satellite data. Conventional approaches of EM induction sounding utilize either the ground observatory datasets (Olsen, 1999c; Guzavina et al, 2019; Munch et al, 2020) or the satellite datasets (Kuvshinov and Olsen, 2006; Püthe and Kuvshinov, 2014). Attempts to incorporate both ground and space observations to invert for the conductivity has been made (Grayver et al, 2017; Kuvshinov et al, 2021; Velímský and Knopp, 2021), also using TFs or fitting time-series of SH coefficients in time domain. The VP/alternating approach framework demonstrated in this study is particularly suitable for accommodating both satellite and observatory magnetic data, and can handle both in a consistent manner together with their respective uncertainties. To achieve this, however, a fully time-domain inversion scheme need to be laid out in prior under the variable projection framework.

5. Conclusions

In this thesis, the task of inducing source and conductivity estimation is posed in the form of a Separable Nonlinear Least Squares (SNLS) problem. By exploiting the inherent property whereby observations depend on source coefficients linearly, whereas the dependency on the subsurface electrical conductivity is non-linear, we proposed a novel inversion scheme that solves the underlying SNLS problem by using the variable projection to determine source and conductivity structures simultaneously. This method was applied to both synthetic tests and real observations. Although the experiments and inversions were limited to ground magnetic field observations and a rather simple 1-D conductivity model parameterization, it is clear that the method is general in both the observational data and the model parameterization aspects. Derivations in Section 2 provide general framework for exploiting the VP and show how conventional inversion schemes that often already implement Jacobians for separate source and conductivity estimation can be reformulated into the SNLS form and solved by using the VP (or alternating) approaches. To gain additional insight into the problem. we studied several variants of the VP and showed their relation to the full joint inversion as well alternating inversion approaches.

The alternating approach provides a simple alternative to the VP method for solving SNLS problems. However, one important aspect that has not been identified in previous studies is that alternating approaches with too rare source model updates can result in deteriorated model estimates along iterations, which eventually undermines the convergence and model recovery. To avoid this, alternating inversions need to perform frequent re-estimation of the inducing source, especially at early stages. Similar to previous studies, a slower convergence of the alternating approaches compared to the full VP method is observed, although this can be compensated in practice by lower computational cost per iteration.

By introducing additional constraints to the joint model space, variable projection methods and alternating approaches prove to be capable of recovering both external field and mantle conductivity simultaneously. They show comparable performance to the Gauss method and transfer function inversion on our (simple) test cases, where potential field assumption is applicable. However, the SNLS problem solved by the VP method is not limited to potential field scenarios. In particular, it can accommodate arbitrary source geometries at arbitrary locations (e.g., current loops, dipoles, SECS); incorporate electric field data as well as both ground and satel-

lite observations. Importantly, VP methods make the explicit use of the physical link (through Maxwell's equations) between the source and conductivity, which preserves consistency between both model spaces. This is in contrast to the conventional approaches where the source and the mantle conductivity are estimated independently and it is often (implicitly) assumed in subsequent transfer function estimation and inversion that the external source estimate is "noise-free". Our synthetic tests showed that even small inconsistencies in a source model can lead to significant artifacts in subsurface conductivity. It is also shown that inadequate modelling of the induced field leads to a biased estimate of the external field structure.

Acknowledgements

The time series of the hourly means at ground magnetic observatories used in this work were taken from the AUX_OBS ESA Swarm product https://earth.esa.int/eogateway/missions/swarm/product-data-handbook/auxiliary-product-definitions, as part of the products maintained by the ESA Swarm DISC and supported by the German Research Foundation, Deutsche Forschungsgemeinschaft, Project number 465486300. The implementation of the code is mostly based on `SciPy` (Virtanen et al, 2020), including the optimization algorithm. We used linear models in the `Scikit-Learn` package (Pedregosa et al, 2011) for robust regressions and the `ChaosMagPy` package (Kloss, 2021) for Q-response calculation.

This work largely stems from an inspirational proposal by my supervisor, Dr. Alexander Grayver, who has since made important contributions to the development of the thesis. Discussions with Alexander have always been pleasant, and inspiring at the same time, often leading to new experiment designs to support an argument or to pinpoint a potential mistake. Prof. Alexey Kuvshinov also provided valuable feedbacks while reviewing the proposal of the project, and despite its novelty, this work finds its concept already in a work published over three decades ago by Alexey and his colleagues.

I am also grateful to Lu Tian and Danyang Jiang, for their support during this project as my close friends, and their valuable opinions from an objective point of view as fellow geophysicists. Lu helped with proofreading and pointed out grammatical issues. Danyang's suggestions on the RMS-misfit phenomenon motivated further modelling, which led to my perception of spectral leakage as the cause.

Bibliography

Aravkin AY, Leeuwen TV (2012) Estimating nuisance parameters in inverse problems. Inverse Problems 28, DOI 10.1088/0266-5611/28/11/115016

Backus G, George B, Parker RL, Parker R, Constable C (1996) Foundations of geomagnetism. Cambridge University Press

Balasis G, Egbert GD (2006) Empirical orthogonal function analysis of magnetic observatory data: Further evidence for nonaxisymmetric magnetospheric sources for satellite induction studies. Geophysical Research Letters 33:2006GL025,721, DOI 10.1029/2006GL025721, URL https://onlinelibrary.wiley.com/doi/10.1029/2006GL025721

Chave AD, Jones AG (2012) The magnetotelluric method: Theory and practice. Cambridge University Press

Conn AR, Gould NIM, Toint PL (2000) Trust Region Methods. Society for Industrial and Applied Mathematics, DOI 10.1137/1.9780898719857, URL https://epubs.siam.org/doi/book/10.1137/1.9780898719857

De Ridder SA, Maddison JR (2018) Full wavefield inversion of ambient seismic noise. Geophysical Journal International 215:1215–1230, DOI 10.1093/GJI/GGY328, URL https://academic.oup.com/gji/article/215/2/1215/5067877

Egbert GD, Kelbert A (2012) Computational recipes for electromagnetic inverse problems. Geophysical Journal International 189, DOI 10.1111/j.1365-246X.2011.05347.x

Egbert GD, Alken P, Maute A, Zhang H (2021) Modelling diurnal variation magnetic fields due to ionospheric currents. Geophysical Journal International 225:1086–1109, DOI 10.1093/gji/ggaa533

Fainberg EB, Kuvshinov AV, Mishina LP, Singer BS (1990) The new approach to global deep sounding. pure and applied geophysics 1990 134:4 134:527–531, DOI 10.1007/BF00878016, URL https://link.springer.com/article/10.1007/BF00878016

Finlay C, Lesur V, Thébault E, Vervelidou F, Morschhauser A, Shore R (2017) Challenges handling magnetospheric and ionospheric signals in internal geomagnetic field modelling. Space Science Reviews 206(1):157–189

Golub G, Pereyra V (2003) Separable nonlinear least squares: The variable projection method and its applications. Inverse Problems 19, DOI 10.1088/0266-5611/19/2/201

Golub GH, Pereyra V (1973) The differentiation of pseudo-inverses and nonlinear least square problems whose variables separate. SIAM J Numer Anal 10, URL https://epubs.siam.org/page/terms

Grayver AV, Munch FD, Kuvshinov AV, Khan A, Sabaka TJ, TøffnerClausen L (2017) Joint inversion of satellitedetected tidal and magnetospheric signals constrains electrical conductivity and water content of the upper mantle and transition zone. Geophysical Research Letters 44:6074–6081, DOI 10.1002/2017GL073446, URL https://onlinelibrary.wiley.com/doi/10.1002/2017GL073446

Grayver AV, Kuvshinov A, Werthmüller D (2021) Time-domain modeling of three-dimensional earth's and planetary electromagnetic induction effect in ground and satellite observations. Journal of Geophysical Research: Space Physics 126:e2020JA028,672, DOI 10.1029/2020JA028672, URL https://agupubs.onlinelibrary.wiley.com/doi/10.1029/2020JA028672

Guzavina M, Grayver A, Kuvshinov A (2019) Probing upper mantle electrical conductivity with daily magnetic variations using global-to-local transfer functions. Geophysical Journal International 219:2125–2147, DOI 10.1093/gji/ggz412

Hansen PC, OLeary DP (1993) The use of the l-curve in the regularization of discrete ill-posed problems. SIAM Journal on Scientific Computing 14:1487–1503, DOI 10.1137/0914086

Hong JH, Zach C, Fitzgibbon A (2017) Revisiting the variable projection method for separable nonlinear least squares problems. Proceedings - 30th IEEE Conference on Computer Vision and Pattern Recognition, CVPR 2017 2017-January:5939–5947, DOI 10.1109/CVPR.2017.629

Hu X, Wei G, Song J, Yang Z, Lu M, Gao L (2021) Full-waveform inversion with source and receiver coupling effects correctionfwi with s-r correction. Geophysics 86:R463–R470, DOI 10.1190/GEO2020-0331.1

Juusola L, Vanhamäki H, Viljanen A, Smirnov M (2020) Induced currents due to 3d ground conductivity play a major role in the interpretation of geomagnetic variations. Annales Geophysicae 38:983–998, DOI 10.5194/angeo-38-983-2020

Kelbert A (2020) The role of global/regional earth conductivity models in natural geomagnetic hazard mitigation. Surveys in Geophysics 41:115–166, DOI 10.1007/s10712-019-09579-z

Kelbert A, Lucas GM (2020) Modified GIC estimation using 3-D earth conductivity. Space Weather 18(8):e2020SW002,467

Kelbert A, Schultz A, Egbert G (2009) Global electromagnetic induction constraints on transition-zone water content variations. Nature 460:1003–1006, DOI 10.1038/nature08257

Kloss C (2021) ancklo/chaosmagpy: Chaosmagpy v0.8. DOI 10.5281/ZENODO.5772527, URL https://doi.org/10.5281/zenodo.5772527#.YemAOHBA6S0.mendeley

Koch S, Kuvshinov A (2013) Global 3-D em inversion of sq variations based on simultaneous source and conductivity determination: Concept validation and resolution studies. Geophysical Journal International 195, DOI 10.1093/gji/ggt227

Kuvshinov A (2012) Deep electromagnetic studies from land, sea, and space: progress status in the past 10 years. Surveys in Geophysics 33(1):169–209

Kuvshinov A, Olsen N (2006) A global model of mantle conductivity derived from 5 years of CHAMP, Ørsted, and SAC-C magnetic data. Geophysical Research Letters 33, DOI 10.1029/2006GL027083, URL https://onlinelibrary.wiley.com/doi/full/10.1029/2006GL027083https://onlinelibrary.wiley.com/doi/abs/10.1029/2006GL027083https://agupubs.onlinelibrary.wiley.com/doi/10.1029/2006GL027083

Kuvshinov A, Grayver A, Tøffner-Clausen L, Olsen N (2021) Probing 3-D electrical conductivity of the mantle using 6 years of Swarm, CryoSat-2 and observatory magnetic data and exploiting matrix Q-responses approach. Earth, Planets and Space 73:67, DOI 10.1186/s40623-020-01341-9, URL https://earth-planets-space.springeropen.com/articles/10.1186/s40623-020-01341-9

Li M, Rickett J, Abubakar A (2013) Application of the variable projection scheme for frequency-domain full-waveform inversionvariable projection scheme for fd-fwi. Geophysics 78:R249–R257, DOI 10.1190/GEO2012-0351.1, URL http://pubs.geoscienceworld.org/geophysics/article-pdf/78/6/R249/3229776/geo2012-0351.pdf

Maus S, Weidelt P (2004) Separating the magnetospheric disturbance magnetic field into external and transient internal contributions using a 1d conductivity model of the earth. Geophysical Research Letters 31, DOI 10.1029/2004GL020232

Munch FD, Grayver AV, Guzavina M, Kuvshinov AV, Khan A (2020) Joint inversion of daily and long-period geomagnetic transfer functions reveals lateral variations in mantle water content. Geophysical Research Letters 47, DOI 10.1029/2020GL087222

Nocedal J, Wright S (2006) Numerical Optimization. Springer, DOI 10.1007/978-0-387-40065-5, URL http://link.springer.com/10.1007/978-0-387-40065-5

O'Leary DP, Rust BW (2013) Variable projection for nonlinear least squares problems. Computational Optimization and Applications 54:579–593, DOI 10.1007/S10589-012-9492-9/TABLES/3, URL https://link.springer.com/article/10.1007/s10589-012-9492-9

Olsen N (1999a) Induction studies with satellite data. Surveys in Geophysics 20:309–340, DOI 10.1023/a:1006611303582

Olsen N (1999b) Induction studies with satellite data. Surveys in Geophysics 1999 20:3 20:309–340, DOI 10.1023/A:1006611303582, URL https://link.springer.com/article/10.1023/A:1006611303582

Olsen N (1999c) Long-period (30 days-1 year) electromagnetic sounding and the electrical conductivity of the lower mantle beneath europe. Geophysical Journal International 138:179–187, DOI 10.1046/J.1365-246X.1999.00854.X/3/138-1-179-FIG006.JPEG, URL https://academic.oup.com/gji/article/138/1/179/640376

Pankratov OV, Kuvshinov AV (2010) Fast calculation of the sensitivity matrix for responses to the earth's conductivity: General strategy and examples. Izvestiya, Physics of the Solid Earth 46:788–804, DOI 10.1134/S1069351310090089

Pedregosa F, Varoquaux G, Gramfort A, Michel V, Thirion B, Grisel O, Blondel M, Prettenhofer P, Weiss R, Dubourg V, Vanderplas J, Passos A, Cournapeau D, Brucher M, Perrot M, Duchesnay E (2011) Scikit-learn: Machine learning in python. Journal of Machine Learning Research 12(85):2825–2830, URL http://jmlr.org/papers/v12/pedregosa11a.html

Pulkkinen A, Amm O, Viljanen A (2003) Ionospheric equivalent current distributions determined with the method of spherical elementary current systems. Journal of Geophysical Research: Space Physics 108(A2)

Püthe C, Kuvshinov A (2014) Mapping 3-D mantle electrical conductivity from space: A new 3-D inversion scheme based on analysis of matrix Q-responses. Geophysical Journal International 197, DOI 10.1093/gji/ggu027

Rickett J (2013) The variable projection method for waveform inversion with an unknown source function. Geophysical Prospecting 61:874–881, DOI 10.1111/1365-2478.12008

Ruhe A, Wedin P (1980) Algorithms for separable nonlinear least squares problems. http://dxdoiorg/101137/1022057 22:318–337, DOI 10.1137/1022057, URL https://epubs.siam.org/doi/abs/10.1137/1022057

Schmucker U (1999) A spherical harmonic analysis of solar daily variations in the years 1964-1965: Response estimates and source fields for global induction-i. methods. Geophysical Journal International 136:439–454, DOI 10.1046/j.1365-246X.1999.00742.x

Sun J, Kelbert A, Egbert GD (2015) Ionospheric current source modeling and global geomagnetic induction using ground geomagnetic observatory data. Journal of Geophysical Research: Solid Earth 120(10):6771–6796

Tsyganenko NA (2019) Secular drift of the auroral ovals: How fast do they actually move? Geophysical Research Letters 46:3017–3023, DOI 10.1029/2019GL082159, URL https://onlinelibrary.wiley.com/doi/abs/10.1029/2019GL082159

Velímský J, Knopp O (2021) Lateral variations of electrical conductivity in the lower mantle constrained by Swarm and CryoSat-2 missions. Earth, Planets and Space 73:4, DOI 10.1186/s40623-020-01334-8, URL https://earth-planets-space.springeropen.com/articles/10.1186/s40623-020-01334-8

Velímský J, Grayver A, Kuvshinov A, achl L (2018) On the modelling of m 2 tidal magnetic signatures: effects of physical approximations and numerical resolution. Earth, Planets and Space 70:192, DOI 10.1186/s40623-018-0967-5, URL https://earth-planets-space.springeropen.com/articles/10.1186/s40623-018-0967-5

Virtanen P, Gommers R, Oliphant TE, Haberland M, Reddy T, Cournapeau D, Burovski E, Peterson P, Weckesser W, Bright J, van der Walt SJ, Brett M, Wilson J, Millman KJ, Mayorov N, Nelson ARJ, Jones E, Kern R, Larson E, Carey CJ, Polat I, Feng Y, Moore EW, VanderPlas J, Laxalde D, Perktold J, Cimrman R, Henriksen I, Quintero EA, Harris CR, Archibald AM, Ribeiro AH, Pedregosa F, van Mulbregt P, SciPy 10 Contributors (2020) SciPy 1.0: Fundamental Algorithms for Scientific Computing in Python. Nature Methods 17:261–272, DOI 10.1038/s41592-019-0686-2

Yamazaki Y, Maute A (2017) Sq and EEJ - a review on the daily variation of the geomagnetic field caused by ionospheric dynamo currents. Space Science Reviews 206:299–405, DOI 10.1007/s11214-016-0282-z

Zenhäusern G, Kuvshinov A, Guzavina M, Maute A (2021) Towards probing earths upper mantle with daily magnetic field variations: exploring a physics-based parametrization of the source. Earth, Planets and Space 73:136, DOI 10.1186/s40623-021-01455-8, URL https://earth-planets-space.springeropen.com/articles/10.1186/s40623-021-01455-8

Zhang H, Egbert GD, Huang Q (2022) A relatively dry mantle transition zone revealed by geomagnetic diurnal variations. Science Advances 8, DOI 10.1126/sciadv.abo3293, URL https://www.science.org/doi/10.1126/sciadv.abo3293

A. Imperfect nature of modelling in windowed Fourier domain

In our synthetic test we observe that although $\chi_{\text{rms}} \approx 1$ can be obtained for the entire dataset, it is not the case with every frequency band (Fig. 3.5). This phenomenon should be attributed to the spectral leakage and as a consequence, the inevitable imperfect nature of windowed-Fourier-domain modelling. In particular, we consider two time series $y(t)$ and $x(t)$, which are related in the frequency domain via

$$Y(\omega) = H(\omega)X(\omega), \tag{A.1}$$

where X, Y are the spectra of x and y, respectively, and $H(\omega)$ is the transfer function. In the general formulation of VP/alternating methods, X and Y correspond to the inducing current parameterization $\mathbf{c}$ and the data vector $\mathbf{d}$, and $H(\omega)$ corresponds to the forward operator $\mathbf{F}(\sigma)$ (Eq. 2.5); in the formulation of Q-response estimation, X and Y are ε_n^m and ι_n^m, respectively, while $H(\omega)$ is nothing but the $Q_n(\omega)$ response (Eq. 2.41). Without loss of generality, we limit ourselves to scalars $X, Y, H \in \mathbb{C}$ in this appendix. The goal here is to show that the windowed spectra of x and y, given by

$$X(\tau,\omega) = \mathscr{F}_{\tau,\omega}[x(t)], \quad Y(\tau,\omega) = \mathscr{F}_{\tau,\omega}[y(t)] \tag{A.2}$$

with the transforms defined in Eq. 2.40 do not strictly satisfy the same relation in the frequency domain. In other words, in general we have

$$Y(\tau,\omega) \neq H(\omega)X(\tau,\omega) \tag{A.3}$$

In this appendix we strictly distinguish between the term windowed Fourier domain and the Fourier domain. The former is defined in Eq. 2.40, and the latter is defined in its continuous form in Eq. 2.2, and in its discrete form as the following convention of the discrete Fourier

transform (DFT) and its inverse (iDFT)

$$\begin{aligned} X(\omega_q) &= \frac{1}{\sqrt{N}} \sum_{k=0}^{N-1} x(t_k)\, e^{-i\omega_q t_k}, \\ x(t_k) &= \frac{1}{\sqrt{N}} \sum_{q=0}^{N-1} X(\omega_q)\, e^{i\omega_q t_k}, \end{aligned} \tag{A.4}$$

where $t_k = k\Delta t$ are the sampling time points, and $\omega_q = q/N\Delta t$ are the frequency points, $k, q = 0, \cdots N-1$. The windowed spectral transform of x in time window τ at frequency ω can be written as

$$\begin{aligned} X(\tau,\omega) &= \frac{1}{\sum_k w_k} \sum_{k\in\{k_\tau\}} w_{k-k_{\tau 0}}\, x(t_k)\, e^{-i\omega(t_k - t_{k_{\tau 0}})} \\ &= \frac{1}{\sum_k w_k} \sum_{k\in\{k_\tau\}} w_{k-k_{\tau 0}} \left[\frac{1}{\sqrt{N}} \sum_{q=0}^{N-1} X(\omega_q) e^{i\omega_q t_k} \right] e^{-i\omega(t_k - t_{k_{\tau 0}})} \\ &= \frac{1}{\sqrt{N}} \sum_{q=0}^{N-1} X(\omega_q) \left[\frac{1}{\sum_k w_k} \sum_{k\in\{k_\tau\}} w_{k-k_{\tau 0}}\, e^{i(\omega_q-\omega)(t_k - t_{k_{\tau 0}})} \right] e^{i\omega_q t_{k_{\tau 0}}} \\ &= \frac{1}{\sqrt{N}} \sum_{q=0}^{N-1} X(\omega_q) \left[\frac{1}{\sum_k w_k} \sum_{p=0}^{K_\tau - 1} w_p\, e^{i(\omega_q-\omega)t_p} \right] e^{i\omega_q t_{k_{\tau 0}}}. \end{aligned} \tag{A.5}$$

Here $k_{\tau 0}$ denotes the first time index of the time window τ, and K_τ the total number of time points in the time window τ. Defining the normalized spectrum of the window function within the time window as

$$\widetilde{W}(\omega) = \frac{1}{\sum_{p=0}^{K_\tau - 1} w_p} \sum_{p=0}^{K_\tau - 1} w_p\, e^{-i\omega t_p}, \tag{A.6}$$

the windowed spectrum of x can be reiterated as

$$X(\tau,\omega) = \frac{1}{\sqrt{N}} \sum_{q=0}^{N-1} X(\omega_q)\, \widetilde{W}(\omega - \omega_q)\, e^{i\omega_q t_{k_{\tau 0}}}. \tag{A.7}$$

The trailing factor $e^{i\omega_q t_{k_{\tau 0}}}$ shifts the phases at respective frequencies to the beginning of the time window. The spectrum $\widetilde{W}$ is normalized as such so that $\widetilde{W}(0) \equiv 1$. In the extreme case of infinite length time series and time windows, we will have $\widetilde{W}(\omega) = \delta(\omega)$, leading to $X(\tau,\omega) \propto X(\omega)$. This is, however, never the case for finite length time series and time windows, where the windowed spectrum at frequency ω always contains the spectrum at adjacent DFT frequencies, i.e. $X(\omega_q)$, a phenomenon known as spectral leakage. Appropriate choices of the window function yield $\widetilde{W}$ that can suppress the leakage, but this phenomenon still exists. The "imperfection" of the forward modelling in windowed Fourier domain becomes clear when we

also write the windowed spectrum of Y in a similar form

$$\begin{aligned} Y(\tau,\omega) &= \frac{1}{\sqrt{N}} \sum_{q=0}^{N-1} Y(\omega_q)\, \widetilde{W}(\omega-\omega_q)\, e^{i\omega_q t k_{\tau 0}} \\ &= \frac{1}{\sqrt{N}} \sum_{q=0}^{N-1} H(\omega_q)\, X(\omega_q)\, \widetilde{W}(\omega-\omega_q)\, e^{i\omega_q t k_{\tau 0}} \end{aligned} \tag{A.8}$$

From Eqs. A.7 and A.8 we see that the $X(\tau,\omega)$ is not simply linked to $Y(\tau,\omega)$ through a product with the transfer function, i.e. Eq. A.3. Only under one specific condition, i.e. $H(\omega) \equiv H_0$, do the two quantities follow the same relation as their Fourier-domain counterparts, as

$$Y(\tau,\omega) = \frac{1}{\sqrt{N}} \sum_{q=0}^{N-1} H_0\, X(\omega_q)\, \widetilde{W}(\omega-\omega_q)\, e^{i\omega_q t k_{\tau 0}} = H_0\, X(\tau,\omega). \tag{A.9}$$

In other words, only when the transfer function has a flat spectrum (the impulse response is pulsive) is the modelling in windowed Fourier domain exactly the same as the modelling in the Fourier domain. Otherwise, the forward modelling as $Y(\tau,\omega) = H(\omega)\, X(\tau,\omega)$ cannot explain the scattering of the data $Y(\tau,\omega)$. This phenomenon should be perceived as an imperfection that affects both the TF estimation, as well as the VP/alternating approaches when using the specific form of forward modelling (Eqs. 2.35 - 2.37). In Q-inversion, this indicates that even for perfect data and synthetic data, there will be residuals in the fitting of $\mathcal{I}$ that cannot be explained by Eq. 2.41. In our implementation of VP/alternating approaches combined with the forward operators (Eq. 2.35 - 2.37), this imperfection manifests itself through the misfits (Fig. 3.5).

B. Supplementary figures

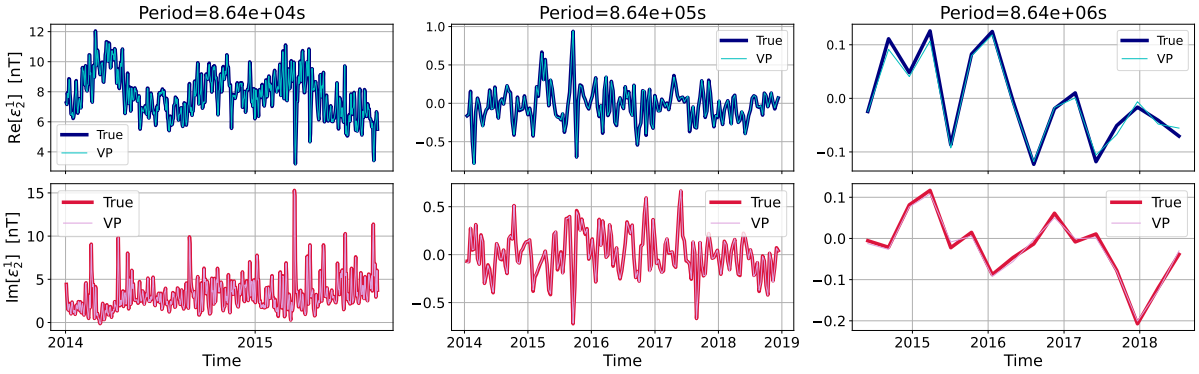

Figure B.1.: Recovered inducing field coefficient ε_2^1 in the frequency domain using alt-Fibonacci scheme. The frequency bands and the legends are the same as Fig. 3.2.

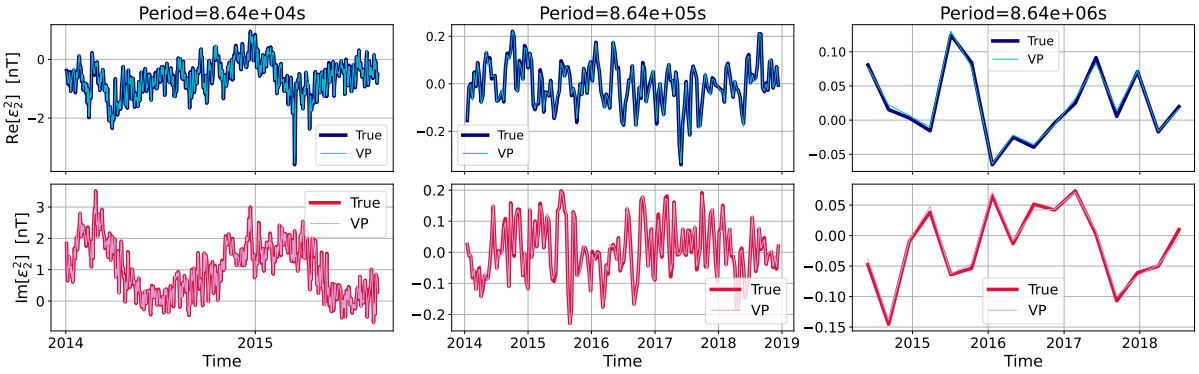

Figure B.2.: Recovered inducing field coefficient ε_2^2 in the frequency domain using alt-Fibonacci scheme. The frequency bands and the legends are the same as Fig. 3.2.

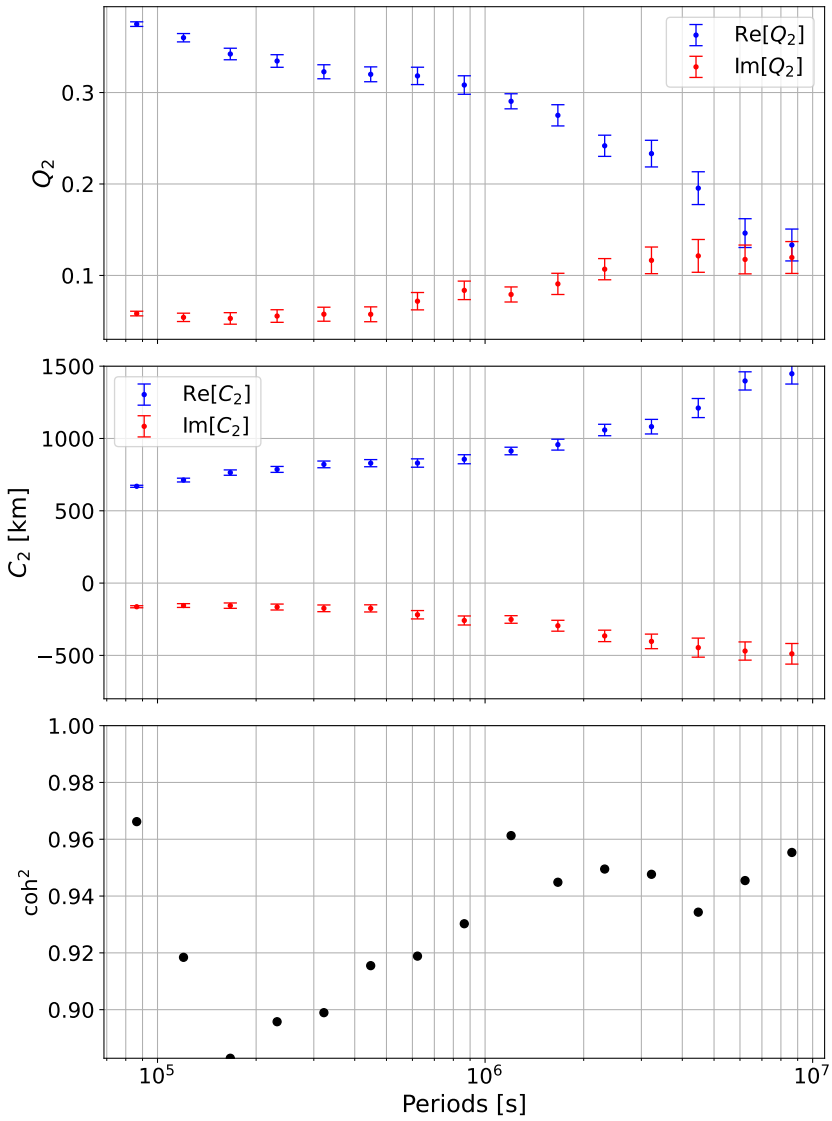

Figure B.3.: Q-responses (top) and C-responses (middle) of degree 2 estimated from SH coefficients of mode $(2, 0)$. The squared coherence of the transfer functions are shown in the bottom panel.

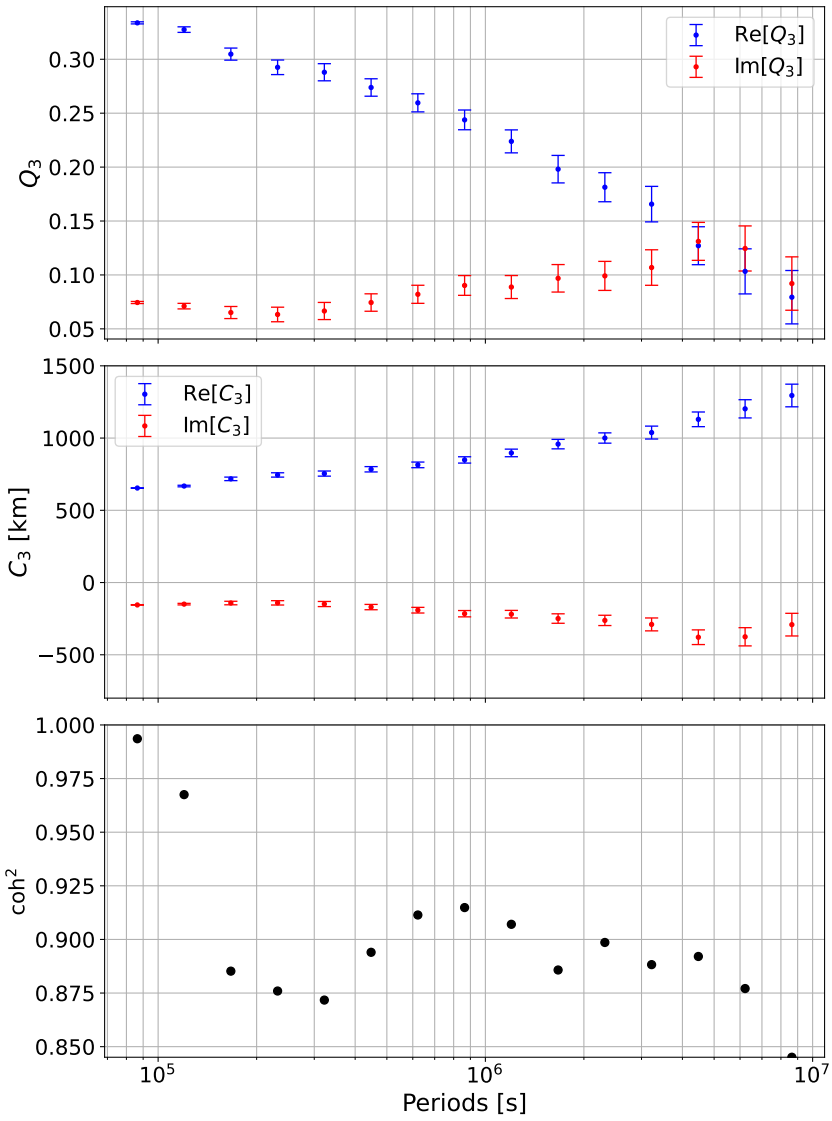

Figure B.4.: Q-responses (top) and C-responses (middle) of degree 3 estimated from SH coefficients of mode $(3, 1)$ from the synthetic dataset. The squared coherence of the transfer functions are shown in the bottom panel.

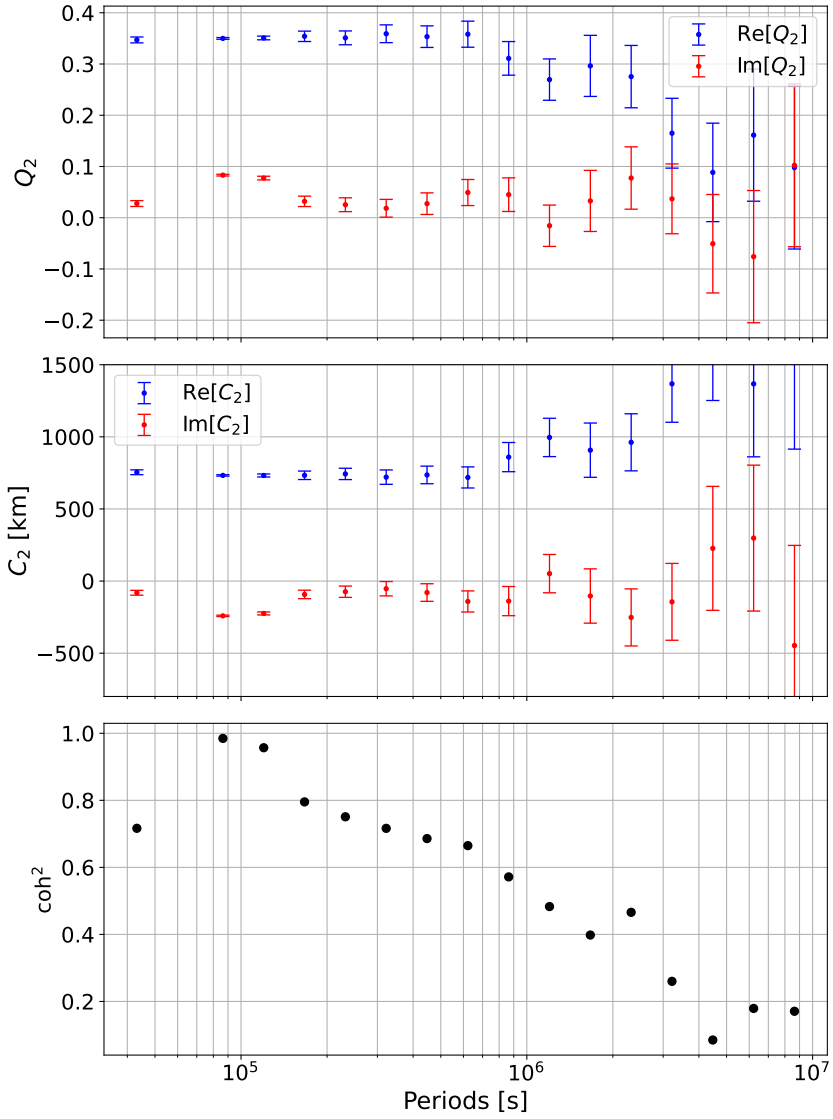

Figure B.5.: Q-responses (top) and C-responses (middle) of degree 2 estimated from SH coefficients of mode $(2, 1)$ from the real dataset. The squared coherence of the transfer functions are shown in the bottom panel.

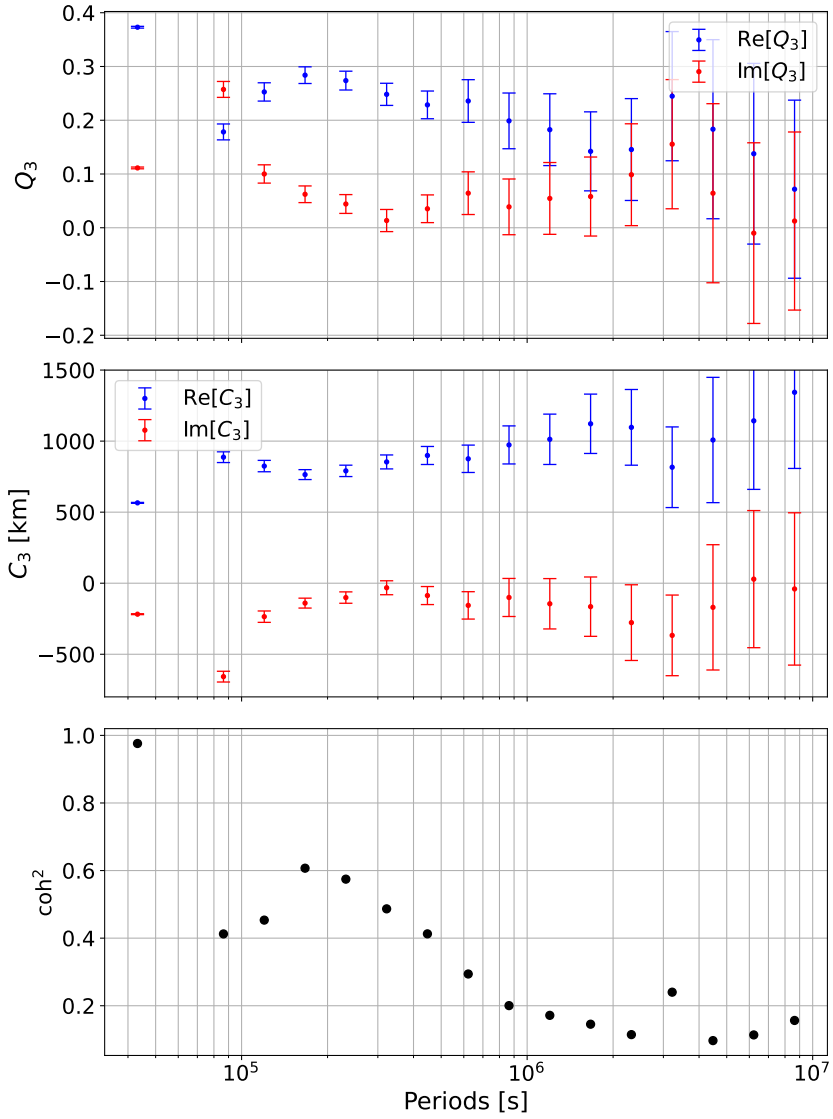

Figure B.6.: Q-responses (top) and C-responses (middle) of degree 3 estimated from SH coefficients of mode $(3, 2)$ from the real dataset. The squared coherence of the transfer functions are shown in the bottom panel.

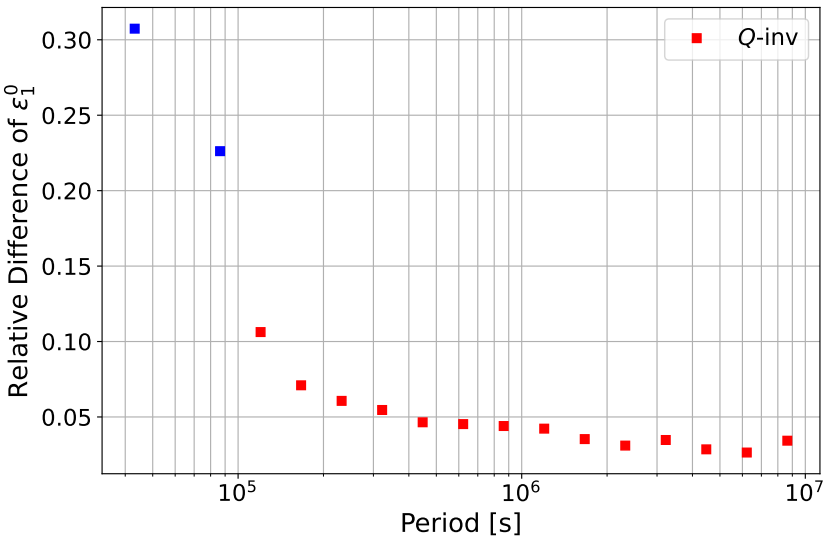

Figure B.7.: Relative differences of inducing field coefficient ε_1^0 between Gauss method and VP inversion. The red squares mark the frequency bands in this SH mode which have a coherence over 0.9 in Q-response estimation, and are thus included in the Q-response inversion.

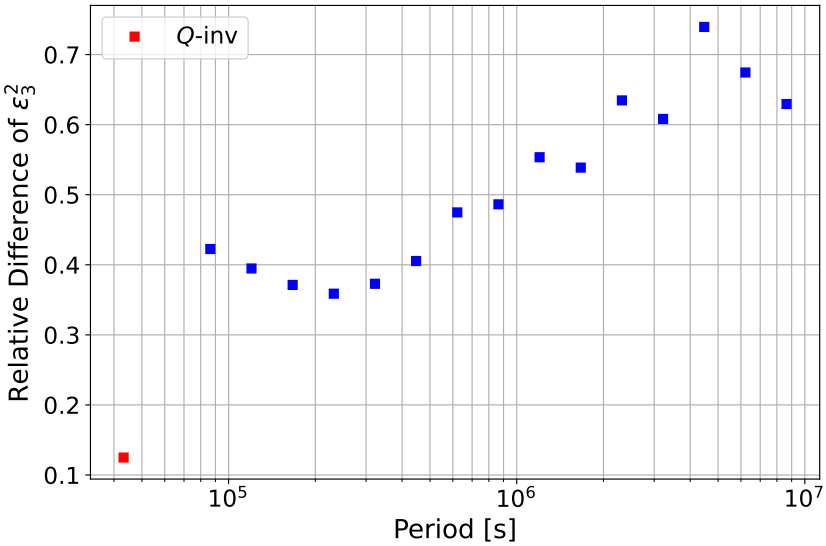

Figure B.8.: Relative differences of inducing field coefficient ε_3^2 between Gauss method and VP inversion. The legends are the same as in Fig. B.7.

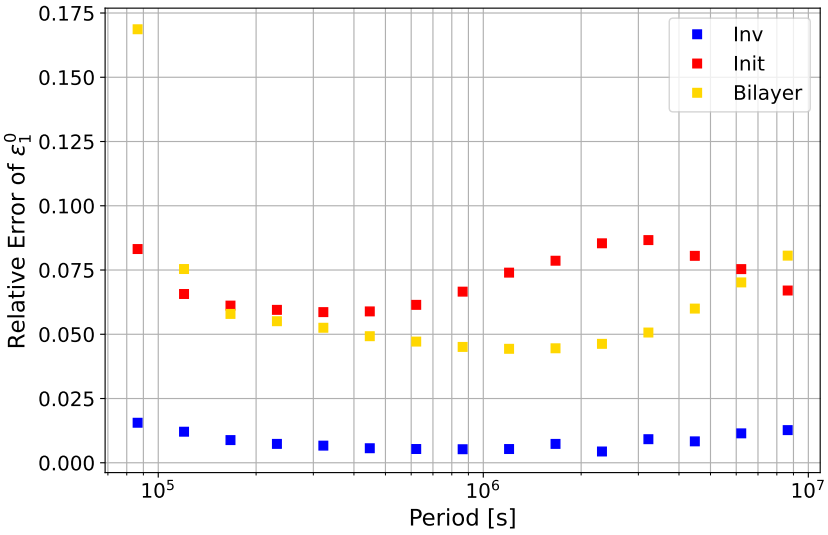

Figure B.9.: Relative errors of the external field coefficients ε_1^0 with different conductivity models. The legends are the same as in Fig. 4.2.

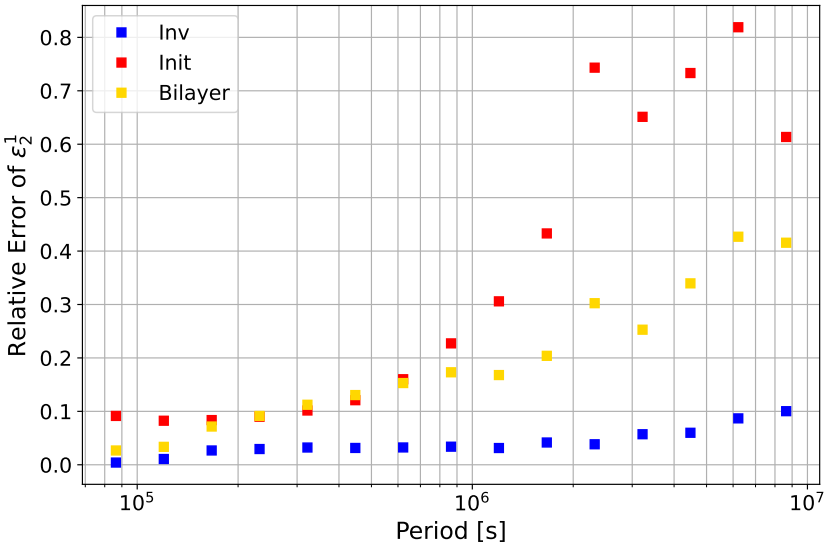

Figure B.10.: Relative errors of the external field coefficients ε_2^1 with different conductivity models. The legends are the same as in Fig. 4.2.

Eidgenössische Technische Hochschule Zürich
Swiss Federal Institute of Technology Zurich

Declaration of originality

The signed declaration of originality is a component of every semester paper, Bachelor's thesis, Master's thesis and any other degree paper undertaken during the course of studies, including the respective electronic versions.

Lecturers may also require a declaration of originality for other written papers compiled for their courses.

I hereby confirm that I am the sole author of the written work here enclosed and that I have compiled it in my own words. Parts excepted are corrections of form and content by the supervisor.

Title of work (in block letters):

SIMULTANEOUS ESTIMATION OF CONDUCTIVITY AND INDUCING FIELD IN ELECTROMAGNETIC INDUCTION SOUNDING

Authored by (in block letters):

For papers written by groups the names of all authors are required.

Name(s):	**First name(s):**
MIN	JINGTAO

With my signature I confirm that

- I have committed none of the forms of plagiarism described in the 'Citation etiquette' information sheet.
- I have documented all methods, data and processes truthfully.
- I have not manipulated any data.
- I have mentioned all persons who were significant facilitators of the work.

I am aware that the work may be screened electronically for plagiarism.

Place, date	**Signature(s)**
Zürich, 22.08.2022	Jingtao Min

For papers written by groups the names of all authors are required. Their signatures collectively guarantee the entire content of the written paper.